

# NAVAL POSTGRADUATE SCHOOL MONTEREY, CALIFORNIA



## THESIS

### BOUNDARY LAYER EFFECTS ON FRONTAL INTERACTION WITH TOPOGRAPHY

by

John H. Powell

June, 1996

Thesis Co-Advisors:

R. T. Williams  
M. S. Peng

Approved for public release; distribution is unlimited.

Thesis  
P7636

DUDLEY KNOX LIBRARY  
NAVAL POSTGRADUATE SCHOOL  
MONTEREY CA 93943-5101

# REPORT DOCUMENTATION PAGE

Form Approved OMB No. 0704-0188

Public reporting burden for this collection of information is estimated to average 1 hour per response, including the time for reviewing instruction, searching existing data sources, gathering and maintaining the data needed, and completing and reviewing the collection of information. Send comments regarding this burden estimate or any other aspect of this collection of information, including suggestions for reducing this burden, to Washington Headquarters Services, Directorate for Information Operations and Reports, 1215 Jefferson Davis Highway, Suite 1204, Arlington, VA 22202-4302, and to the Office of Management and Budget, Paperwork Reduction Project (0704-0188) Washington DC 20503.

1. AGENCY USE ONLY (Leave blank)	2. REPORT DATE June 1996.	3. REPORT TYPE AND DATES COVERED Master's Thesis	
4. TITLE AND SUBTITLE BOUNDARY LAYER EFFECTS ON FRONTAL INTERACTION WITH TOPOGRAPHY		5. FUNDING NUMBERS	
6. AUTHOR(S) Powell, John H.			
7. PERFORMING ORGANIZATION NAME(S) AND ADDRESS(ES) Naval Postgraduate School Monterey CA 93943-5000		8. PERFORMING ORGANIZATION REPORT NUMBER	
9. SPONSORING/MONITORING AGENCY NAME(S) AND ADDRESS(ES)		10. SPONSORING/MONITORING AGENCY REPORT NUMBER	
11. SUPPLEMENTARY NOTES The views expressed in this thesis are those of the author and do not reflect the official policy or position of the Department of Defense or the U.S. Government.			
12a. DISTRIBUTION/AVAILABILITY STATEMENT Approved for public release; distribution is unlimited.		12b. DISTRIBUTION CODE	
13. ABSTRACT (maximum 200 words) A hydrostatic, primitive equation model with frontogenetical deformation forcing is used to simulate the passage of cold fronts over a two-dimensional ridge. The model includes a K-theory planetary boundary layer (PBL) parameterization with implicitly defined diffusion coefficients. Numerical simulations are performed for synoptic-scale ridges of varying widths both with and without frontal forcing. These results are compared to simulations that do not include a PBL parameterization, similar to previous inviscid studies by Williams et al. Relative to the inviscid results, the PBL simulations produced reduced frontolysis on the upwind slope and reduced frontogenesis on the lee slope, resulting in significantly smaller frontogenetic variations over the mountain. This is caused by convergence forcing in the well-mixed layer offsetting the overall frontolytical forcing on the upwind slope, and greatly reduced lee side convergence forcing due to the PBL. In contrast to the inviscid results, the final downstream front is weaker in the mountain simulations than in the flat-topography control case when PBL effects are included. In all PBL simulations, gravity wave generation is greatly reduced and no lee side hydraulic jumps are observed. In general, the inclusion of a PBL into the model results in more realistic wind and temperature fields compared to the inviscid model simulations.			
14. SUBJECT TERMS frontogenesis, numerical simulation, topography, boundary layer, K closure, semi-geostrophic		15. NUMBER OF PAGES 76	
		16. PRICE CODE	
17. SECURITY CLASSIFI- CATION OF REPORT Unclassified	18. SECURITY CLASSIFI- CATION OF THIS PAGE Unclassified	19. SECURITY CLASSIFI- CATION OF ABSTRACT Unclassified	20. LIMITATION OF ABSTRACT UL

NSN 7540-01-280-5500

Standard Form 298 (Rev. 2-89)  
Prescribed by ANSI Std. Z39-18 298-102



**Approved for public release; distribution is unlimited.**

**BOUNDARY LAYER EFFECTS ON FRONTAL INTERACTION  
WITH TOPOGRAPHY**

John H. Powell  
Lieutenant Commander, United States Navy  
B.S., University of Colorado, 1986

Submitted in partial fulfillment  
of the requirements for the degree of

**MASTER OF SCIENCE IN METEOROLOGY AND PHYSICAL  
OCEANOGRAPHY**

from the

**NAVAL POSTGRADUATE SCHOOL  
June 1996**





## ABSTRACT

A hydrostatic, primitive equation model with frontogenetical deformation forcing is used to simulate the passage of cold fronts over a two-dimensional ridge. The model includes a K-theory planetary boundary layer (PBL) parameterization with implicitly defined diffusion coefficients. Numerical simulations are performed for synoptic-scale ridges of varying widths both with and without frontal forcing. These results are compared to simulations that do not include a PBL parameterization, similar to previous inviscid studies by Williams et al.

Relative to the inviscid results, the PBL simulations produced reduced frontolysis on the upwind slope and reduced frontogenesis on the lee slope, resulting in significantly smaller frontogenetic variations over the mountain. This is caused by convergence forcing in the well-mixed layer offsetting the overall frontolytical forcing on the upwind slope, and greatly reduced lee side convergence forcing due to the PBL. In contrast to the inviscid results, the final downstream front is weaker in the mountain simulations than in the flat-topography control case when PBL effects are included. In all PBL simulations, gravity wave generation is greatly reduced and no lee side hydraulic jumps are observed. In general, the inclusion of a PBL into the model results in more realistic wind and temperature fields compared to the inviscid model simulations.

## CONTENTS

1. Introduction	1
2. The structure of the book	3
3. The structure of the book	3
4. The structure of the book	3
5. The structure of the book	3
6. The structure of the book	3
7. The structure of the book	3
8. The structure of the book	3
9. The structure of the book	3
10. The structure of the book	3
11. The structure of the book	3
12. The structure of the book	3
13. The structure of the book	3
14. The structure of the book	3
15. The structure of the book	3
16. The structure of the book	3
17. The structure of the book	3
18. The structure of the book	3
19. The structure of the book	3
20. The structure of the book	3
21. The structure of the book	3
22. The structure of the book	3
23. The structure of the book	3
24. The structure of the book	3
25. The structure of the book	3
26. The structure of the book	3
27. The structure of the book	3
28. The structure of the book	3
29. The structure of the book	3
30. The structure of the book	3
31. The structure of the book	3
32. The structure of the book	3
33. The structure of the book	3
34. The structure of the book	3
35. The structure of the book	3
36. The structure of the book	3
37. The structure of the book	3
38. The structure of the book	3
39. The structure of the book	3
40. The structure of the book	3
41. The structure of the book	3
42. The structure of the book	3
43. The structure of the book	3
44. The structure of the book	3
45. The structure of the book	3
46. The structure of the book	3
47. The structure of the book	3
48. The structure of the book	3
49. The structure of the book	3
50. The structure of the book	3
51. The structure of the book	3
52. The structure of the book	3
53. The structure of the book	3
54. The structure of the book	3
55. The structure of the book	3
56. The structure of the book	3
57. The structure of the book	3
58. The structure of the book	3
59. The structure of the book	3
60. The structure of the book	3
61. The structure of the book	3
62. The structure of the book	3
63. The structure of the book	3
64. The structure of the book	3
65. The structure of the book	3
66. The structure of the book	3
67. The structure of the book	3
68. The structure of the book	3
69. The structure of the book	3
70. The structure of the book	3
71. The structure of the book	3
72. The structure of the book	3
73. The structure of the book	3
74. The structure of the book	3
75. The structure of the book	3
76. The structure of the book	3
77. The structure of the book	3
78. The structure of the book	3
79. The structure of the book	3
80. The structure of the book	3
81. The structure of the book	3
82. The structure of the book	3
83. The structure of the book	3
84. The structure of the book	3
85. The structure of the book	3
86. The structure of the book	3
87. The structure of the book	3
88. The structure of the book	3
89. The structure of the book	3
90. The structure of the book	3
91. The structure of the book	3
92. The structure of the book	3
93. The structure of the book	3
94. The structure of the book	3
95. The structure of the book	3
96. The structure of the book	3
97. The structure of the book	3
98. The structure of the book	3
99. The structure of the book	3
100. The structure of the book	3



## TABLE OF CONTENTS

I. INTRODUCTION .....	1
II. MODEL DEVELOPMENT .....	7
A. BASIC EQUATIONS .....	7
1. Inviscid Model Formulation .....	7
2. Boundary Layer Formulation .....	13
B. COMPUTATIONAL ASPECTS .....	16
III. NUMERICAL SOLUTIONS .....	21
A. FRONTAL SOLUTIONS WITH NO TOPOGRAPHY .....	21
B. NON-FRONTAL SOLUTIONS WITH TOPOGRAPHY .....	26
C. FRONTAL SOLUTIONS WITH TOPOGRAPHY .....	40
1. Intensity Variations .....	40
2. Frontogenetical Forcing .....	52
IV. SUMMARY OF RESULTS .....	61
LIST OF REFERENCES .....	65
INITIAL DISTRIBUTION LIST .....	67



## I. INTRODUCTION

Mountainous topography introduces dynamical complications to meteorological phenomena on all scales, from sub-mesoscale systems to the global circulation. Some effects such as diurnal mountain and valley winds are produced by the differential diabatic heating typically associated with mountainous terrain. Local wind regimes are also profoundly affected by sub-synoptic scale variations in topography. However, many important synoptic and mesoscale effects are related directly to the dynamics of atmospheric flow over synoptic-scale mountains. These effects include lee cyclogenesis, mountain wave generation, and downslope wind storms such as the *Mistral* in the southern French Alps. Equally important to forecasters is the effect of mountainous topography on atmospheric frontal intensity. Forecasters have long known that fronts tend to weaken as they move up the windward slope of a mountain range and often intensify on the lee slope. This effect has been documented in quantitative observational studies, for example in the analyses of high-resolution Alpine Experiment (ALPEX) data of Hartsough and Blumen (1990) and Radinovic (1986).

Analytical solutions to the problem of fronts moving over mountain ridges are difficult because of the importance of ageostrophic circulations and the resulting nonlinearity of the equations of motion. Bannon (1983) derives frontal solutions for a quasigeostrophic front passing over a two-dimensional ridge. The linear Boussinesq equations he employs do not allow dynamic interaction with the mountain-forced circulations, but the results show windward slope weakening and lee slope strengthening of the cold front nonetheless. This is a result of the superposition of the mountain-forced

temperature field with that of the front. Bannon (1984) shows the effect of dynamic ageostrophic interactions in semigeostrophic solutions, but solutions are only obtained when the topography is allowed to vary in time. Blumen and Gross (1987) examine the effect of mountain dynamics by treating the front as passive scalar fields advected over a two-dimensional ridge by semigeostrophic steady-state fields. The scalar fields represent the temperature and tangential wind fields of a weak front. The solutions show the frontolytical effect of mountain-forced upwind divergence and the frontogenetical effect of lee side convergence. Other studies examine the dynamics of frontal interaction with topography by considering simple two-fluid models of the atmosphere (Davies 1984 and Blumen 1992).

While important realistic effects can be resolved by simplified analytical treatments, the full dynamics of frontal interaction with topography are analytically intractable. Furthermore, the simplified analytical solutions are only useful over the limited range of flow parameters for which the steady-state solutions are valid. Davies' (1984) solutions, for example, are valid over a limited range of front-mountain aspect ratios. Pierrehumbert and Wyman (1985) characterize stratified flow over a ridge by the Rossby number ( $Ro$ ) and a non-dimensional height parameter ( $\hat{h}$ ) of the mountain. They show that for small values of  $Ro$  and  $\hat{h}$ , solutions based on the semigeostrophic approximations are valid. As  $\hat{h}$  increases to near a critical height, however, the approximations break down and the flow exhibits vertically propagating gravity waves and a hydraulic jump on the lee side (Williams et al. 1992). Clearly, frontal solutions based on semigeostrophic flow are inaccurate for these flows.

Numerical simulation provides a means to investigate the dynamics of flows without analytical solutions. Zehnder and Bannon (1988) uses a semigeostrophic numerical model to study the effect of a front moving over a two-dimensional ridge toward a stationary downstream deformation field. The nonlinear mountain interactions are isolated and shown to produce a weakening frontal zone on the windward slope and intensification on the lee slope. This effect is attributed to temperature field deformation by mountain-forced convergence/divergence patterns.

Williams et al. (1992) perform similar simulations using a two-dimensional primitive equation (PE) Boussinesq model. In these experiments a horizontal deformation field is applied to a thermal wind balanced disturbance superposed on a steady-state semigeostrophic mountain solution. The deformation field is allowed to move over the ridge with the mean background flow. The mountain-forced convergence/divergence fields produce frontogenetic variations similar to those found by Zehnder and Bannon. Both frontal and non-frontal simulations are performed over a range of mountain widths. The wider mountain non-frontal solutions vary little from the semigeostrophic initial state, but the steeper mountains produce vertically propagating gravity waves and lee side hydraulic jumps. This wave activity is amplified in the frontal simulations. Williams et al. also run the model without the deformation forcing to show the mountain effects on a passive tracer field similar to that considered by Blumen and Gross (1987). The passive temperature field gradient decreases on the windward side and increases on the lee side. In both the passive and forced frontal experiments, the mountain effect on frontal intensity is largely symmetrical (except for lee side gravity wave activity). In the passive



simulations, the final downstream intensity is nearly equal to the initial intensity and in the forced simulations, the final intensity in the mountain cases is similar to that of the flat topography case.

A similar PE model is used by Gross (1994) to simulate a three-dimensional front passing over a finite, isolated synoptic-scale ridge. The front is produced by a developing nonlinear baroclinic wave moving over the ridge. In addition to demonstrating anti-cyclonic deformation of the frontal zone and horizontal flow diversion around the ridge, the study reveals three-dimensional effects relevant to cross-ridge flow. For low Froude number flows in which the flow is not blocked, the trailing synoptic anticyclone is impeded by the ridge, producing a cross-ridge pressure gradient. Down-gradient acceleration of the lee slope winds causes increased convergence and frontogenesis downwind of the ridge. Horizontal shear deformation is shown to have a small effect on frontal forcing over the ridge. Generally, however, the cross-mountain effects on the front agree well with the two-dimensional simulations of Williams et al. (1992).

All of these studies consider inviscid flows only. While it is widely recognized that the planetary boundary layer (PBL) can have important effects on flow over topography, few studies address the problem quantitatively. Carruthers and Hunt (1990) review the effects of a uniform PBL capped by a strong inversion on the stratified overlying flow based on the linear analysis of Hunt et al. (1988) and the nonlinear analysis of Carruthers and Choularton (1982). Variations in the inversion height across the ridge are predicted, the nature of which depend on the Froude numbers at and above the inversion layer. The presence of a varying elevated inversion significantly affects the

mountain-forced flow accelerations within the PBL. The diffusive and momentum transfer effects of the PBL are not considered.

Yang (1993) simulates two-dimensional stratified flow over a bell-shaped ridge using both hydrostatic and nonhydrostatic models with a turbulent kinetic energy (TKE) boundary layer parameterization. Large amplitude vertically propagating gravity waves are produced in both models and trapped lee waves are observed in the nonhydrostatic simulations. Abrupt hydraulic effects are not observed, however, except on extremely steep mesoscale ridges (slopes with height to length aspect ratios approaching 1.0). The study also shows that the hydrostatic and nonhydrostatic models produce similar flow structures when the length scale of the ridge is much larger than a flow parameter defined as  $U/N$ , where  $U$  is the mean velocity scale and  $N$  is the Brunt-Väisälä frequency.

The effect of the PBL has been treated in greater detail in flat topography frontal studies. Keyser and Anthes (1982) investigate PBL effects on frontogenesis using a two-dimensional hydrostatic PE model incorporating a mult-layer, first-order K-theory PBL parameterization. Detailed realistic frontal features not produced in inviscid simulations are evident in the PBL model results. The model is also run with a simple one-layer bulk drag PBL parameterization. The multi-layer K-theory PBL model is shown to produce more realistic results than either the bulk parameterization or the Ekman formulation used by Blumen (1980) in a similar model. Dunst and Rhodin (1990) obtain similar detail in their frontal simulations using a high-resolution first-order parameterization similar to the one used by Keyser and Anthes (1982), but with a different diffusion coefficient formulation.



This study seeks to improve the physical accuracy of previous numerical studies on frontal interaction with topography by including a realistic PBL parameterization. The basic model is the two-dimensional Boussinesq PE model of Williams et al. (1992, denoted W92) with the inclusion of a first order K-theory PBL parameterization following Keyser and Anthes (1982, denoted KA82). Numerous PBL closure schemes are evaluated by Holt and Raman (1988), who find that while the overall turbulence structure of the atmosphere is better modelled by more complex turbulent kinetic energy closure schemes, the mean structure of PBL is fairly insensitive to the closure scheme employed. The KA82 formulation is similar to the modified Djolov (1973) mixing length parameterization reviewed. In a separate study (publication pending), Peng and Williams compare the results of frontal simulations over flat topography using the KA82 formulation to those using the Dunst and Rhodin (1990) approach. The two PBL parameterizations again produce very similar results.

As in W92, the model is applied to infinite north-south ridges of varying widths. The simulations are run both with and without frontal deformation forcing in both inviscid and PBL modes. In most cases, model parameters are selected to correspond to those of W92 to facilitate comparison. The basic model and PBL formulations are developed in Chapter II. Model solutions are presented and discussed in Chapter III, and the results are summarized in Chapter IV.

## II. MODEL DEVELOPMENT

### A. BASIC EQUATIONS

This study uses the W92 model modified by Peng and Williams to include a boundary layer formulation following KA82. Development of the inviscid equations in the following section follows W92.

#### 1. Inviscid Model Formulation

The model is based on the adiabatic primitive equations with hydrostatic and Boussinesq approximations applied, which neglect the compressibility of the atmosphere. The domain is two-dimensional in  $x$  and  $z$  and is perpendicular to the semi-infinite ridge. Rotational effects are included in an  $f$ -plane approximation, and velocity and temperature fields are considered constant in  $y$ . This results in increasing errors as the equations are integrated in time, but W92 shows that neglecting along-front variations is a valid approximation in this frontogenesis study. The upper boundary is a rigid lid and the horizontal boundaries are cyclic.

The equations of motion are modelled using a terrain-following vertical coordinate  $\zeta$  defined as

$$\zeta = \frac{z - z_s}{Z} \quad (1)$$

where  $z_s$  is the surface height,  $H$  is the height of the upper boundary and  $Z = H - z_s$ . This

coordinate system places the lower boundary at  $\zeta = 0$  and the upper boundary at  $\zeta = 1$ .

The Boussinesq equations (Ogura and Philips 1962) are transformed with equation (1) to give

$$\frac{\partial \mathbf{V}}{\partial t} + \mathbf{V} \cdot \nabla \mathbf{V} + \zeta \frac{\partial \mathbf{V}}{\partial \zeta} = -\nabla \phi - \frac{g}{\theta_0} (\zeta - 1) \theta \nabla Z - f \mathbf{k} \times \mathbf{V} + \mathbf{F}, \quad (2)$$

$$\frac{\partial \theta}{\partial t} + \mathbf{V} \cdot \nabla \theta + \zeta \frac{\partial \theta}{\partial \zeta} = Q, \quad (3)$$

$$\nabla \cdot (Z \mathbf{V}) + Z \frac{\partial \zeta}{\partial \zeta} = 0, \quad (4)$$

$$\frac{\partial \phi}{\partial \zeta} = \frac{g}{\theta_0} Z \theta, \quad (5)$$

where

$$\theta = T(p_0/p)^\kappa - \theta_0, \quad (6)$$

$$\phi = \theta_0 [c_p (p_0/p)^\kappa + gZ/\theta_0 - c_p]. \quad (7)$$

In these equations,  $\nabla$  is the horizontal gradient operator on  $\zeta$  level surfaces.  $\mathbf{F}$  and  $Q$  are

fourth-order diffusion terms for momentum and potential temperature, included to damp numerical noise in the inviscid model. The diffusion terms also balance the frontal forcing in steady-state to prevent sub-grid scale frontal collapse. They include terms of the form

$$F_{Hu} = -K_H \frac{\partial^4 u}{\partial x^4}, \quad (8)$$

$$F_{vu} = -K_v \frac{\partial^4 u}{\partial \zeta^4}, \quad (9)$$

representing horizontal and vertical diffusion, with similar terms for  $v$  and  $\theta$ .  $Q$  also represents the dry convective adjustment process. Coefficients  $K_H$  and  $K_v$  are given simple vertical profiles in the inviscid model. Other symbols have the usual meteorological meaning. Vertical boundary conditions are

$$\dot{\zeta} = 0 \quad \text{applied at} \quad \zeta = 0, 1. \quad (10)$$

Horizontal boundary conditions are periodic.

The frontogenesis simulations are forced by the vertically uniform horizontal wind deformation field

$$\begin{aligned} U_d &= (D/\mu) \cosh(\mu y) \cos[\mu(x - Ut) + x_1], \\ V_d &= (D/\mu) \sinh(\mu y) \sin[\mu(x - Ut) + x_1], \end{aligned} \quad (11)$$

where  $D$ ,  $\mu = 2\pi/W$ , and  $x_l$  are constants and  $U$  is the mean background flow. This deformation field is cyclic in  $x$  and moves with the mean flow. It is also nondivergent and irrotational.

The dependent variables can be expanded into mean, deformation, and perturbation components as follows:

$$\begin{aligned}
\mathbf{V} = & \{ \alpha [U + U_d(x - Ut, y)] + u(x, \zeta, t) \} \mathbf{i} \\
& + \{ \alpha V_d(x - Ut, y) + v(x, \zeta, t) \} \mathbf{j}, \\
\dot{\zeta} = & \dot{\zeta}(x, \zeta, t), \\
\theta = & \theta(x, \zeta, t), \\
\phi = & \Phi_d(x - Ut, y) - fUy + \varphi(x, \zeta, t),
\end{aligned} \tag{12}$$

where

$$\alpha = \langle Z \rangle / Z. \tag{13}$$

The brackets ( $\langle \rangle$ ) indicate a horizontal average over the domain and  $\alpha$  is factor accounting for the effect of atmospheric thickness variations on the mean and deformation flows. The deformation pressure function  $\Phi_d$  maintains the geostrophic balance of the deformation flow.

Equations (2) - (5) can be put in flux form by multiplying equations (2) and (3) by  $Z$  and substituting from equation (4), using the vector identity

$$\nabla \cdot (A \mathbf{V}) = A \nabla \cdot \mathbf{V} + (\nabla A) \cdot \mathbf{V}, \tag{14}$$

where  $A$  is a scalar. Substituting the variable forms of equations (12) and evaluating at  $y = 0$  yields

$$\begin{aligned}
Z \frac{\partial u}{\partial t} + \frac{\partial}{\partial x} [Z(\alpha U + u)^2] + \frac{\partial}{\partial \zeta} [Z(\alpha U + u) \dot{\zeta}] + Z \frac{\partial}{\partial x} [\alpha U_d (\alpha U + u)] \\
- Z \alpha U \frac{\partial U_d}{\partial x} + Z \frac{\partial \varphi}{\partial x} - \frac{g(\zeta - 1)\theta}{\theta_0} Z \frac{\partial Z}{\partial x} - f_v Z - Z F_u = 0,
\end{aligned} \tag{15}$$

$$\begin{aligned}
Z \frac{\partial v}{\partial t} + \frac{\partial}{\partial x} [Z(\alpha U + u)v] + \frac{\partial}{\partial \zeta} (Zv \dot{\zeta}) + Z \alpha U_d \frac{\partial v}{\partial x} \\
- v \frac{\partial}{\partial x} (Z \alpha U_d) - Z f U + f(\alpha U + u) Z - Z F_v = 0,
\end{aligned} \tag{16}$$

$$Z \frac{\partial \theta}{\partial t} + \frac{\partial}{\partial x} [Z(\alpha U + u)\theta] + \frac{\partial}{\partial \zeta} (Z\theta \dot{\zeta}) + Z \alpha U_d \frac{\partial \theta}{\partial x} - Z Q = 0, \tag{17}$$

$$\frac{\partial}{\partial x} [Z(\alpha U + u)] + Z \frac{\partial \dot{\zeta}}{\partial \zeta} = 0, \tag{18}$$

$$\frac{\partial \varphi}{\partial \zeta} = \frac{g}{\theta_0} Z \theta. \tag{19}$$

The pressure perturbation  $\varphi$  must be eliminated to close this system of equations.

Integrating equation (19) over  $\zeta$  yields



$$\varphi = \varphi_0 + \varphi_s, \quad (20)$$

where

$$\varphi_s = \int_0^\zeta \frac{g}{\theta_0} \theta Z d\zeta, \quad (21)$$

and  $\varphi_0$  is the surface value. Equation (18) is then integrated from  $\zeta = 0$  to  $\zeta = 1$  to give

$$\frac{\partial}{\partial x}(\overline{uZ}) = 0, \quad (22)$$

where the overbar indicates vertical integration over the entire domain. To obtain a closed form we also assume that the mass flux does not vary in time so that

$$(\overline{uZ}) = (\overline{uZ})_{t=0}. \quad (23)$$

This assumption neglects the effect of mountain wave drag and the loss of mean flow momentum to the boundary layer. These minor losses are assumed to be offset by large-scale forcing and are not explicitly included in the model.

The pressure function form of equation (20) is introduced into equation (15) to give

$$Z \frac{\partial u}{\partial t} = -L - Z \frac{\partial \varphi_0}{\partial x} - Z \frac{\partial \varphi_s}{\partial x} + \frac{g(\zeta - 1)\theta}{\theta_0} Z \frac{\partial Z}{\partial x} + f v Z + Z F_u, \quad (24)$$



where  $L$  contains the momentum flux terms in equation (15). Finally, we apply the constant mass flux assumption of equation (23) to the vertical average of equation (24) and subtract the result from equation (24), giving

$$Z \frac{\partial u}{\partial t} = -L + \bar{L} - Z \frac{\partial}{\partial x} (\varphi_s - \bar{\varphi}_s) + \frac{g}{\theta_0} [(\zeta - 1)\theta - \overline{(\zeta - 1)\theta}] Z \frac{\partial Z}{\partial x} + f(v - \bar{v})Z + Z(F_u - \bar{F}_u). \quad (25)$$

Equation (25) provides a prognostic equation for  $u$  in terms of  $V$  and  $\theta$ . The model is based on the numerical integration of equations (25), (16) and (17) in time.

## 2. Boundary Layer Formulation

The boundary layer parameterization employed follows KA82, which is based on the high-resolution nocturnal PBL parameterization of Blackadar (1978). Turbulent fluxes are represented in K theory by

$$\overline{u'w'} = -K_{mz} \frac{\partial u}{\partial z}, \quad (26)$$

$$\overline{v'w'} = -K_{mz} \frac{\partial v}{\partial z}, \quad (27)$$

$$\overline{w'\theta'} = -K_{\theta z} \frac{\partial \theta}{\partial z}. \quad (28)$$

The diffusion coefficients  $K_{mz}$  and  $K_{\theta z}$  are calculated implicitly from model shear and stability fields to minimize *a priori* assumptions about the boundary layer structure. Blackadar (1978) derives a closed system of equations for calculating  $K_{mz}$  and  $K_{\theta z}$  based on the second-order closure scheme of Mellor and Yamada (1974). He adapts the Mellor and Yamada “level-2” approximation, which neglects advective and diffusive terms in the second moment turbulence equations, such that the equations obey Monin-Obukov similarity. The equations are solved in terms of the mixing length  $l$ , vertical shear  $s$ , and the Richardson number  $Ri$ , given by

$$Ri = \frac{g}{\theta} \frac{\partial \theta}{\partial z} \frac{1}{s^2} \quad (29)$$

$$s = \left| \frac{\partial V}{\partial z} \right|.$$

In this formulation,  $l$  is not explicitly calculated and must be specified based on empirical evidence of the mixing length above the surface layer. Over the range of positive and slightly negative  $Ri$ , the resulting distribution is approximated by

$$K_{mz} = K_{\theta z} = \begin{cases} 1.1(l^2 s) \left( \frac{Ri_c - Ri}{Ri_c} \right), & Ri < Ri_c \\ 0, & Ri \geq Ri_c \end{cases} \quad (30)$$

where the critical Richardson number  $Ri_c = 0.25$  (Blackadar, 1978). Note that the vertical shear dependence is included in  $Ri$ . Following KA82, the coefficients are broken down into a small, constant diffusive part  $K_{z0}$  and a variable part modelled after equation (30):

$$K_{mz} = K_{\theta z} = \begin{cases} K_{z0} + k_0^2 l_s^2 \left( \frac{Ri_c - Ri}{Ri_c} \right), & Ri < Ri_c \\ K_{z0}, & Ri \geq Ri_c \end{cases} \quad (31)$$

where  $k_0$  is the von Karman constant.

This formulation defines the vertical fluxes of heat and momentum above the surface layer, which is assumed to be contained within the first model layer. The surface layer fluxes are modelled after Monin-Obukov similarity theory, which gives

$$\overline{u'w'} = - \frac{u_*^2 u}{(u^2 + v^2)^{1/2}}, \quad (32)$$

$$\overline{v'w'} = - \frac{u_*^2 v}{(u^2 + v^2)^{1/2}},$$

$$\overline{w'\theta'} = 0, \quad (33)$$

where

$$u_* = \frac{k_0 (u^2 + v^2)^{1/2}}{\ln(z/z_0) - \psi_m}. \quad (34)$$

Here  $z_0$  is the surface roughness length (the height at which velocity decreases to zero) and  $\psi_m$  is the surface layer stability correction term. Diabatic surface heating is not included in the model, giving the lower boundary condition of equation (33) and requiring a neutral surface layer so that  $\psi_m = 0$ . Other constants are listed in Table 1. In equations (32) through (34)  $u$  and  $v$  are the velocities at the first model level and  $z$  is the corresponding height.

Given the turbulent fluxes computed from equations (26) through (28) and (32) through (34), the basic momentum and heat equations are modified by adding the terms

$$-\frac{\partial(\overline{u'w'})}{\partial\zeta}\mathbf{i} - \frac{\partial(\overline{v'w'})}{\partial\zeta}\mathbf{j}, \text{ and } -\frac{\partial(\overline{w'\theta'})}{\partial\zeta} \quad (35)$$

to the right hand sides of equations (2) and (3), respectively. The fourth-order diffusion coefficients in equations (8) and (9) are also modified as described in the next section.

## B. COMPUTATIONAL ASPECTS

The model equations are solved numerically using finite differencing on an Arakawa B grid (Arakawa and Lamb, 1977). Temperature, pressure, and vertical velocity points are offset horizontally from horizontal momentum points, and vertical velocity points are also offset vertically. Finite differences are centered in space and time, with a Matsuno scheme (Euler backward) time step inserted every fourth iteration to control solution separation. Convective adjustment is applied every three time steps by vertically averaging the potential temperature field in areas of static instability. The model domain extends 3600 km in the east-west ( $x$ ) direction and 12 km vertically. Horizontal grid

**Table 1.** Specification of constant parameters.

Parameter	Numerical value	Parameter	Numerical value
$W$	3600 km	$Ri_c$	1
$H$	12 km	$k_0$	0.4
$\Delta x$	40 km	$K_0$	$1.4 \times 10^{11} \text{ m}^4 \text{ s}^{-1}$
$\Delta \zeta$	1/50	$K_{H0}$	$10^5 \text{ m}^2 \text{ s}^{-1}$
$\Delta t$	90 s	$K_{z0}$	$1 \text{ m}^2 \text{ s}^{-1}$
$h$	2 km	$z_0$	0.4 m
$U$	$10 \text{ m s}^{-1}$	$l$	100 m
$D$	$10^{-5} \text{ s}^{-1}$	$f$	$10^{-4} \text{ s}^{-1}$
$\partial\Theta_s/\partial z$	$4 \text{ K km}^{-1}$	$g$	$9.8 \text{ m s}^{-1}$
$a$	12 K	$c_p$	$1003 \text{ m}^2 \text{ s}^{-2} \text{ K}^{-1}$
$\mu$	$1.75 \times 10^{-3} \text{ km}^{-1}$	$\theta_0$	300 K
$x_I$	$-\pi$	$p_0$	1000 mb
$\zeta_T$	0.75		

spacing is 40 km and there are 50 vertical levels uniformly spaced in  $z$ , corresponding to 240 m spacing over flat topography. The time increment is 90 s. Other numerical constants are listed in Table 1. The surface topography is defined by

$$z_s = h \cos^2 \left[ \frac{\pi(x - W/2)}{\epsilon W} \right], \quad |x - W/2| \leq \frac{\epsilon W}{2}. \quad (36)$$

The mountain height  $h$  is held constant while the width  $\epsilon$  (the fraction of the horizontal domain occupied by the mountain) is varied between 0.6 and 0.2.



Fourth-order diffusion constants in the inviscid model are given the value  $K_0$  at the surface and increase linearly in the vertical to a factor of 10 at the upper boundary. The linear increase is included to maximize the damping of small-scale numerical noise throughout the domain without including excessive surface diffusion. A hyperbolic sponge layer is also included near the top of the domain. The output fields show little damping of resolved waves and the sponge layer effectively eliminates reflection off the upper boundary. In the PBL model, the fourth-order diffusion coefficients are defined following KA82 as

$$K_H = (\Delta x)^2 \left\{ K_{H0} + \frac{1}{2} k_0^2 (\Delta x)^2 \left[ \left( \frac{\partial u}{\partial x} \right)^2 + \left( \frac{\partial v}{\partial x} \right)^2 \right]^{1/2} \right\}. \quad (37)$$

Vertical and horizontal diffusion coefficients for  $u$ ,  $v$  and  $\theta$  are given equal values within each model.

Boundary layer diffusion is computed using equations (31) through (35), with the constant values given in Table 1. Finite differencing tends to give systematically greater values of  $Ri$  than the mean  $Ri$  within the layer (Blackadar, 1978), so  $Ri_c = 1.0$  vice the theoretical value of 0.25 to account for the finite grid resolution (following KA82).

Initial fields are the same as those used in W92. The non-frontal mountain initial flow is defined by semigeostrophic solutions (following Merkin, 1975) for constant  $U$  and stratification away from the ridge and periodic boundary conditions. In frontal simulations, a perturbation is added to these basic fields, defined by

$$\theta_{t=0} = \frac{\partial \theta_s}{\partial z} [Z(\zeta - 1) + H/2] - \begin{cases} a \cos(\mu x + x_1) \cos^2 \left( \frac{\zeta \pi}{2\zeta_T} \right), & \zeta \leq \zeta_T \\ 0. & \zeta > \zeta_T \end{cases} \quad (38)$$

Here  $\partial \theta_s / \partial z$  is the basic field stratification and  $a$  is the perturbation amplitude. Note that the perturbation is limited to the lower part of the domain (below  $\zeta_T$ ) to prevent frontogenesis at the upper boundary. It is also offset horizontally ( $x_1$ ) such that the maximum perturbation coincides with the axis of dilatation of the deformation field (equation (11)). Initial  $u$ ,  $v$  and  $w$  fields are derived using the thermal wind, quasigeostrophic circulation, and continuity equations. Details are given in W92.





### III. NUMERICAL SOLUTIONS

The results of the numerical simulations are presented and discussed in the following sections. In each case, the inviscid data are similar to those presented in W92, which provides a complete discussion of these results. The emphasis of this study is the comparison of the inviscid case results to those of the PBL simulations, which are integrated from the same initial conditions.

#### A. FRONTAL SOLUTIONS WITH NO TOPOGRAPHY

The model is run first with no topography to serve as a control case for the mountain simulations. The initial fields are shown in Figure 1 as functions of  $x$  and  $z$ . The cross-frontal velocity field in Figure 1b (and all subsequent figures) includes the mean background flow  $U$  but not the constant deformation field component. At time  $t = 0$ , the axis of dilatation of the deformation field is coincident with the maximum surface temperature gradient at  $x = 900$  km. The stretching deformation, which moves with the background flow, will therefore intensify this cold frontal zone.

Figure 2 contains the frontal solutions after 48 hours of integration. Only the lower part of the atmosphere is shown to highlight near-surface effects. The front has intensified and all fields have been advected downstream with the background current. These fields clearly show the maximum thermal gradient and associated vorticity maxima at the surface, decreasing rapidly with height. The corresponding PBL solutions are shown in Figure 3. Strong vertical mixing is evident in the near-vertical potential temperature contours throughout the 1.0 to 1.2 km well-mixed layer. The frontal zone

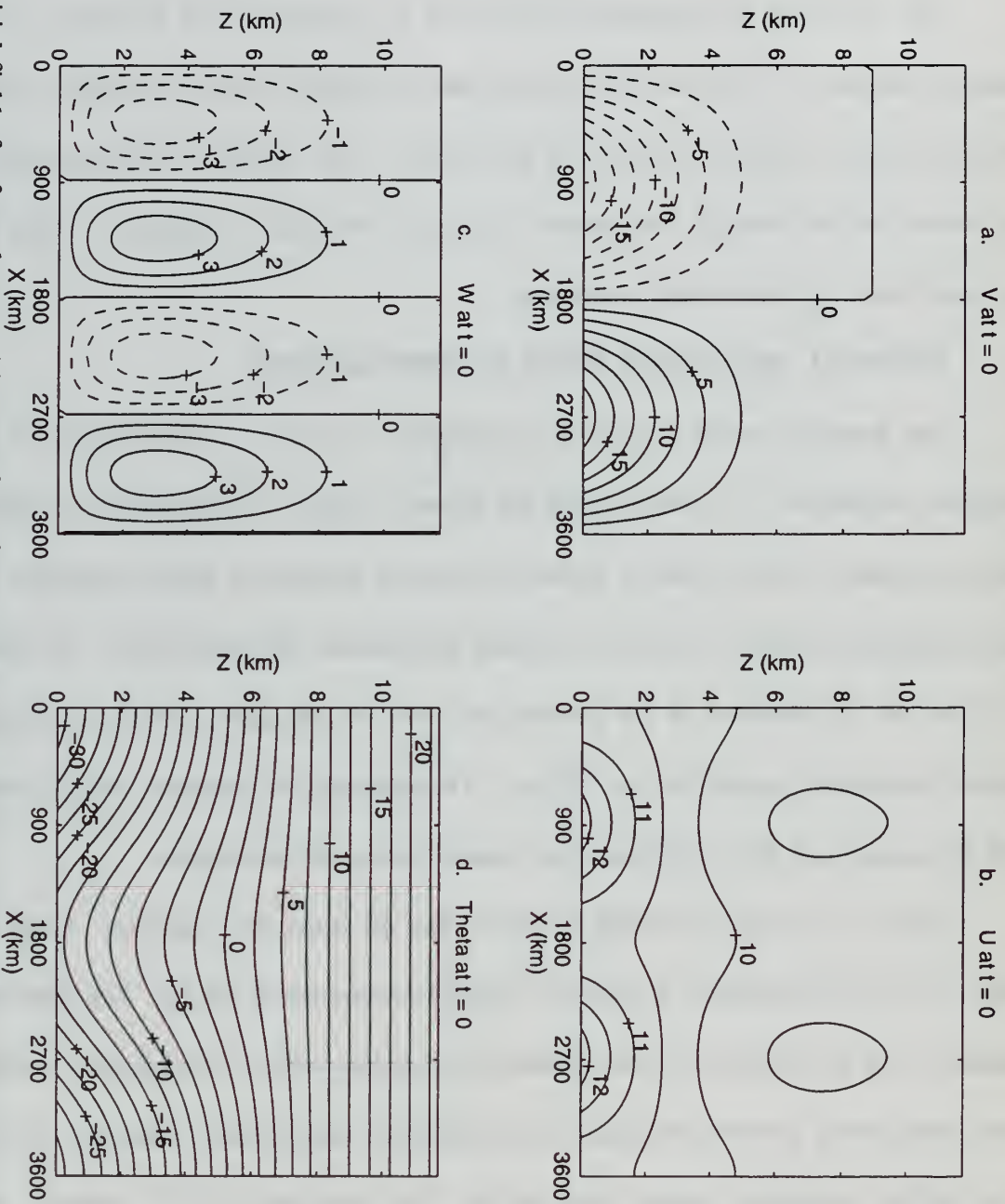


**Figure 1.** Initial fields for frontal case: (a) along-front flow, m/s; (b) cross-front flow, m/s; (c) vertical velocity,  $10^{-3}$  m/s; (d) potential temperature, deg C.

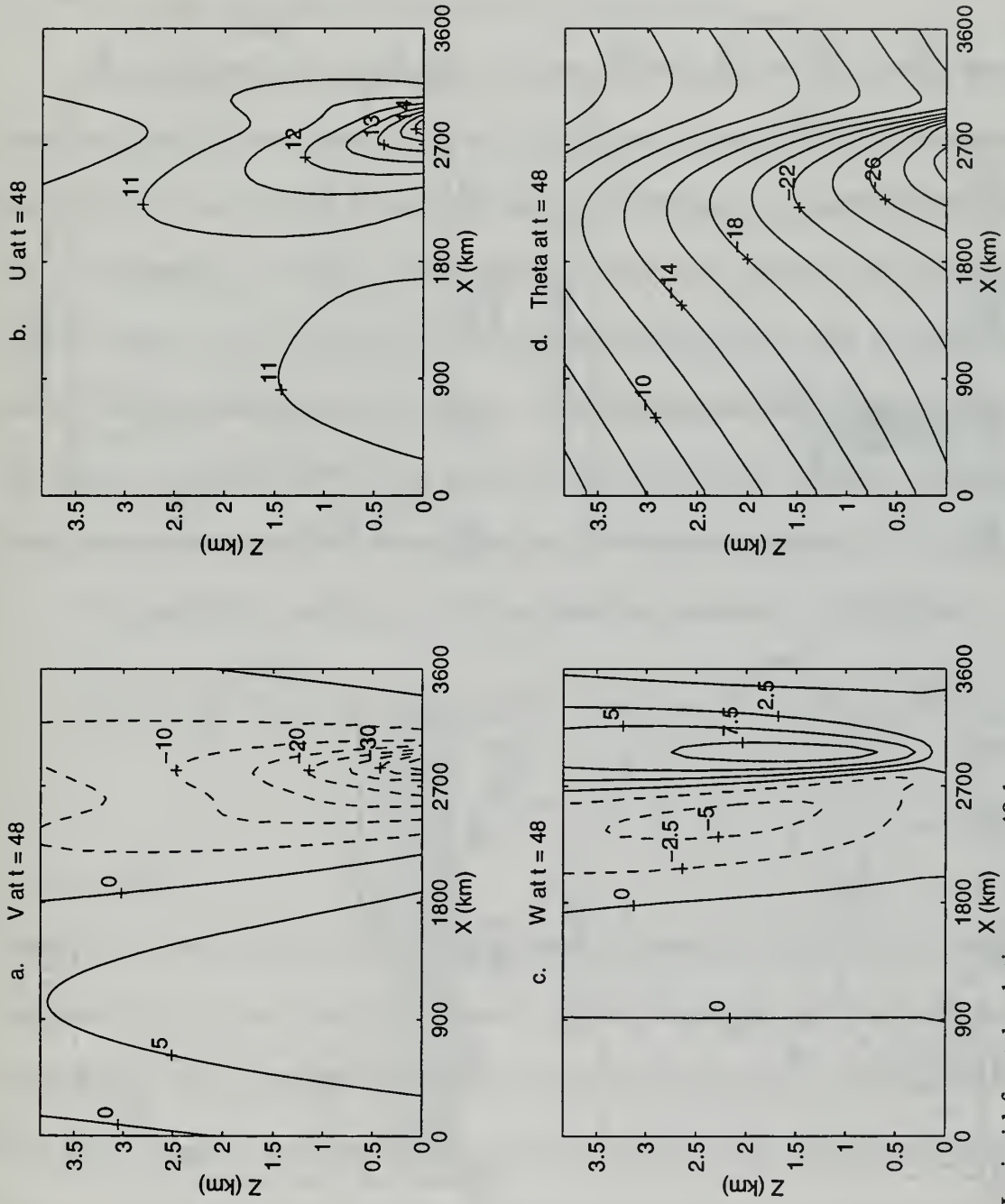


**Figure 2.** Inviscid frontal solutions at  $t = 48$  h.

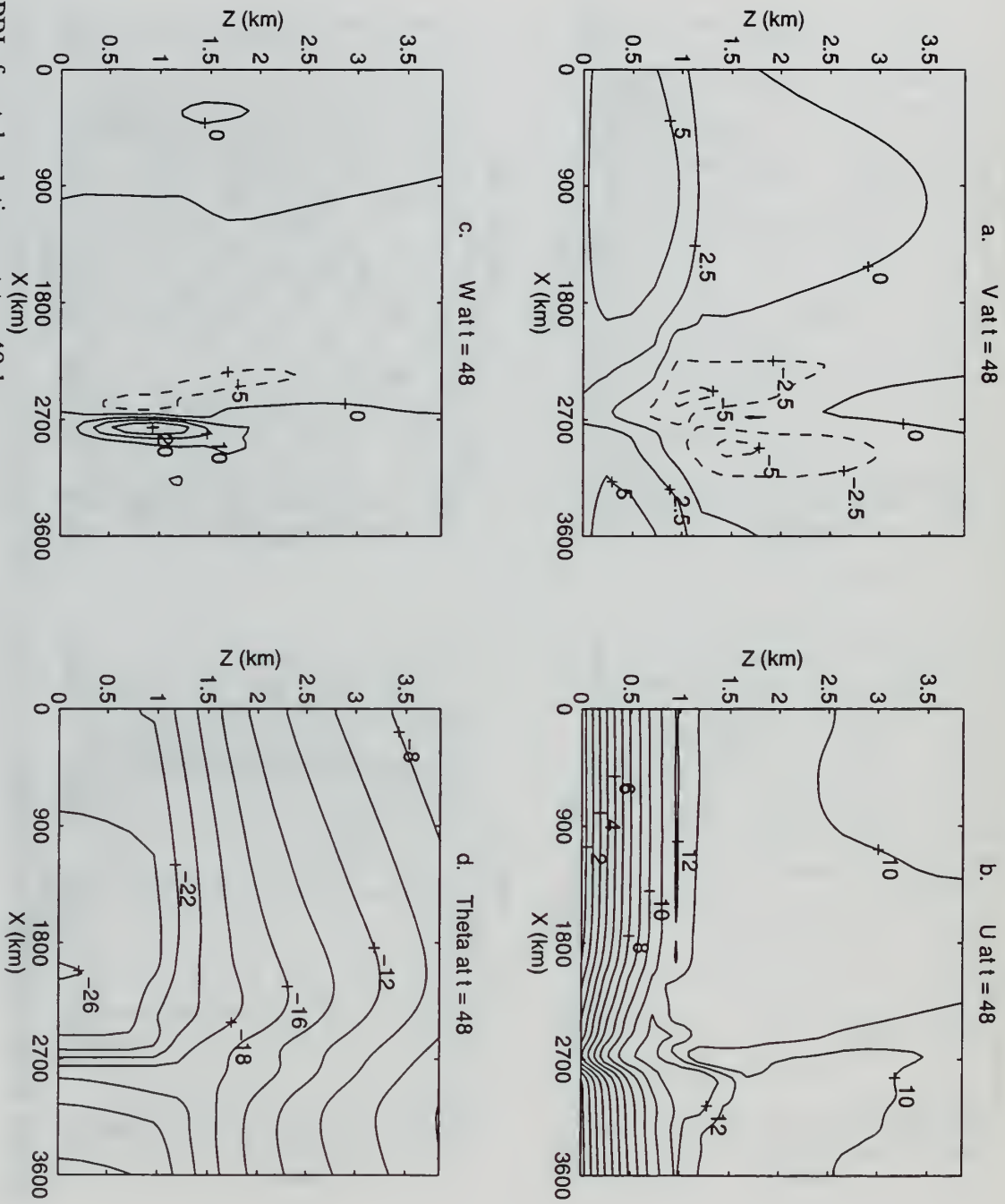


Figure 3. PBL frontal solutions at  $t = 48$  h.



is weaker than that shown in Figure 2, and the thermal gradient is constant throughout the PBL. Here the cross-front and along-front wind maxima are elevated jets near the top of the PBL as winds are frictionally forced to zero at the surface.

In a separate study (discussed in Chapter I), Peng and Williams obtain frontal solutions similar to those shown in Figure 3. Employing a variable horizontal coordinate, they present a more detailed depiction of the frontal structure. A major finding is that the simulated fronts are always weaker when PBL effects are included, due primarily to vertical mixing. The turbulent mixing of the weaker-gradient upper PBL air reduces the potential temperature gradient at the surface. This effect can be seen in Figures 2 and 3. The PBL also produces diffusion in addition to the fourth-order diffusion, resulting in further smoothing of the fields and a reduction of the thermal gradient.

To quantify the strength of the frontal zone, the parameter  $d$  is defined as

$$d = \frac{|\Delta\theta|}{\left| \frac{\partial\theta}{\partial x} \right|_{\max}}, \quad (39)$$

where  $\Delta\theta$  is the maximum horizontal potential temperature variation on the lowest numerical level. The temporal evolution of the  $d$ -value for the flat topography simulations is shown in Figure 4. After an initial period of reduced frontogenesis, the PBL front undergoes frontogenesis at a rate nearly equal to that of the inviscid front (indicated by the slopes of the curves in Figure 4) until about 36 h, when it reaches

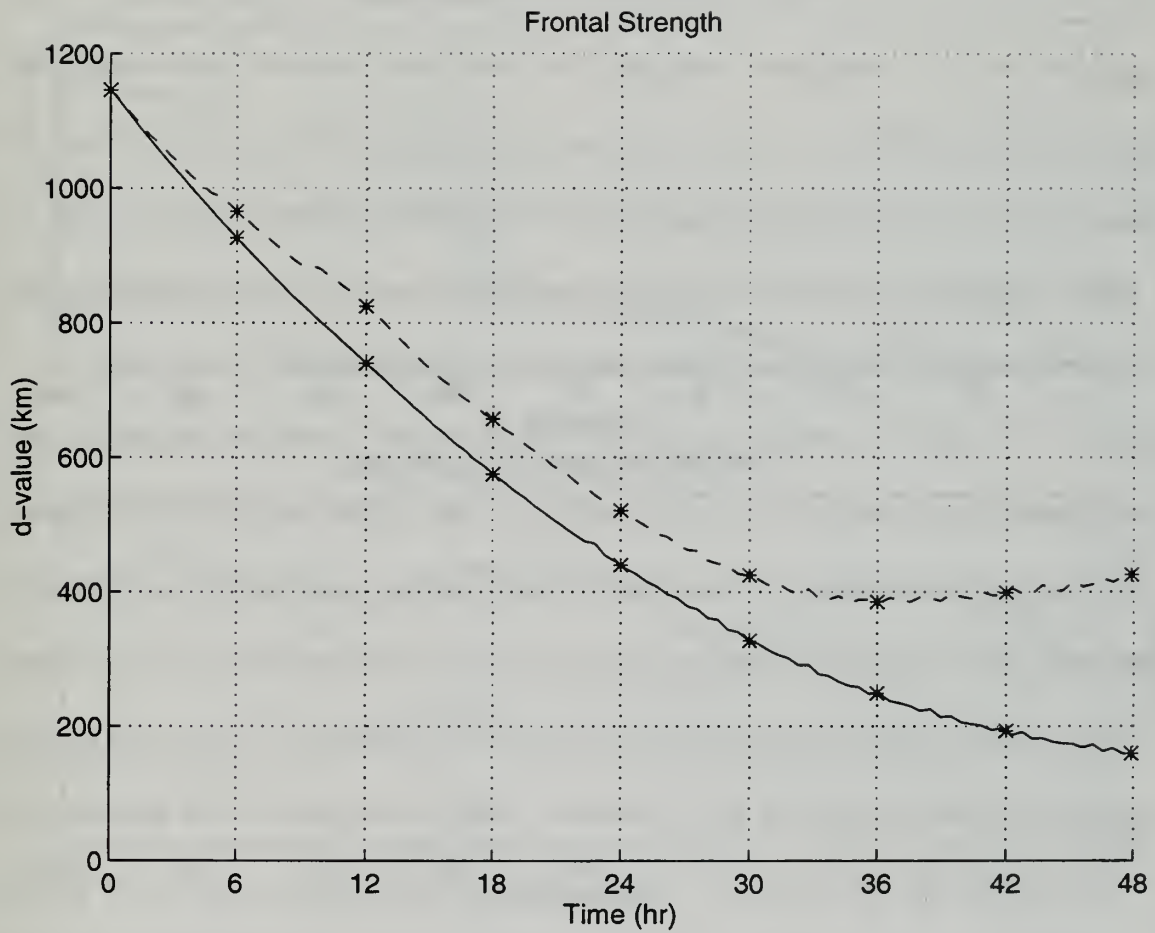
maximum intensity. At this point the frontogenetical forcing is matched by the diffusive forcing and the front is in steady-state. The curves in Figure 4 will be used as a benchmark for the mountain simulations.

The front in the PBL case also translates slower than the frictionless front, which is over 200 km further downstream at  $t = 48$  h. The difference between the frontal positions (defined by the location of maximum potential temperature gradient) is shown as a function of time in Figure 5a. The increase in the distance that the PBL front lags behind is correlated to the difference in maximum cross-frontal velocities (Figure 5b). The velocities shown are vertical averages over the four lowest numerical levels (equivalent to 960 m) and are representative of the average PBL cross-frontal wind at the frontal surface. The fronts are separated by no more than 50 km through  $t = 18$  h, when the velocities are similar. After  $t = 18$  h, the velocities diverge and the frontal separation steadily increases. Thus it appears that the reduction of the cross-frontal wind velocity caused by the PBL results in a slower translation speed and a different vertical tilt. Because the deformation field moves with the background flow, however, it is expected that both fronts will eventually move with the same speed. Clearly, vertical mixing in the PBL plays a role in the causing the PBL surface front to lag behind the inviscid front.

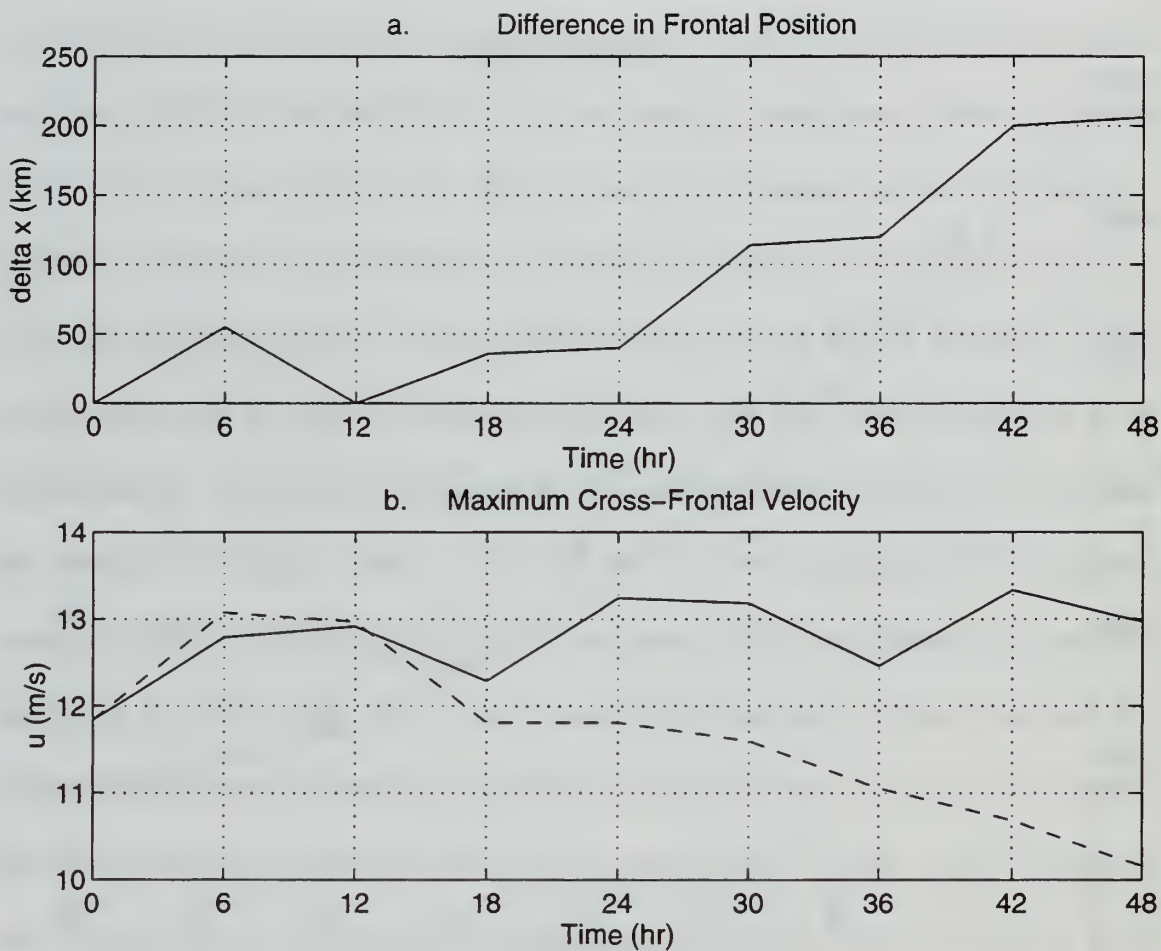
## **B. NON-FRONTAL SOLUTIONS WITH TOPOGRAPHY**

Before investigating topographic effects on the fronts, the effects of the PBL on the basic flow over the ridge must be examined. In these experiments, the semigeostrophic initial fields are integrated in time with no temperature perturbation or deformation forcing applied. The initial fields for the  $\epsilon = 0.6$  ridge are shown in





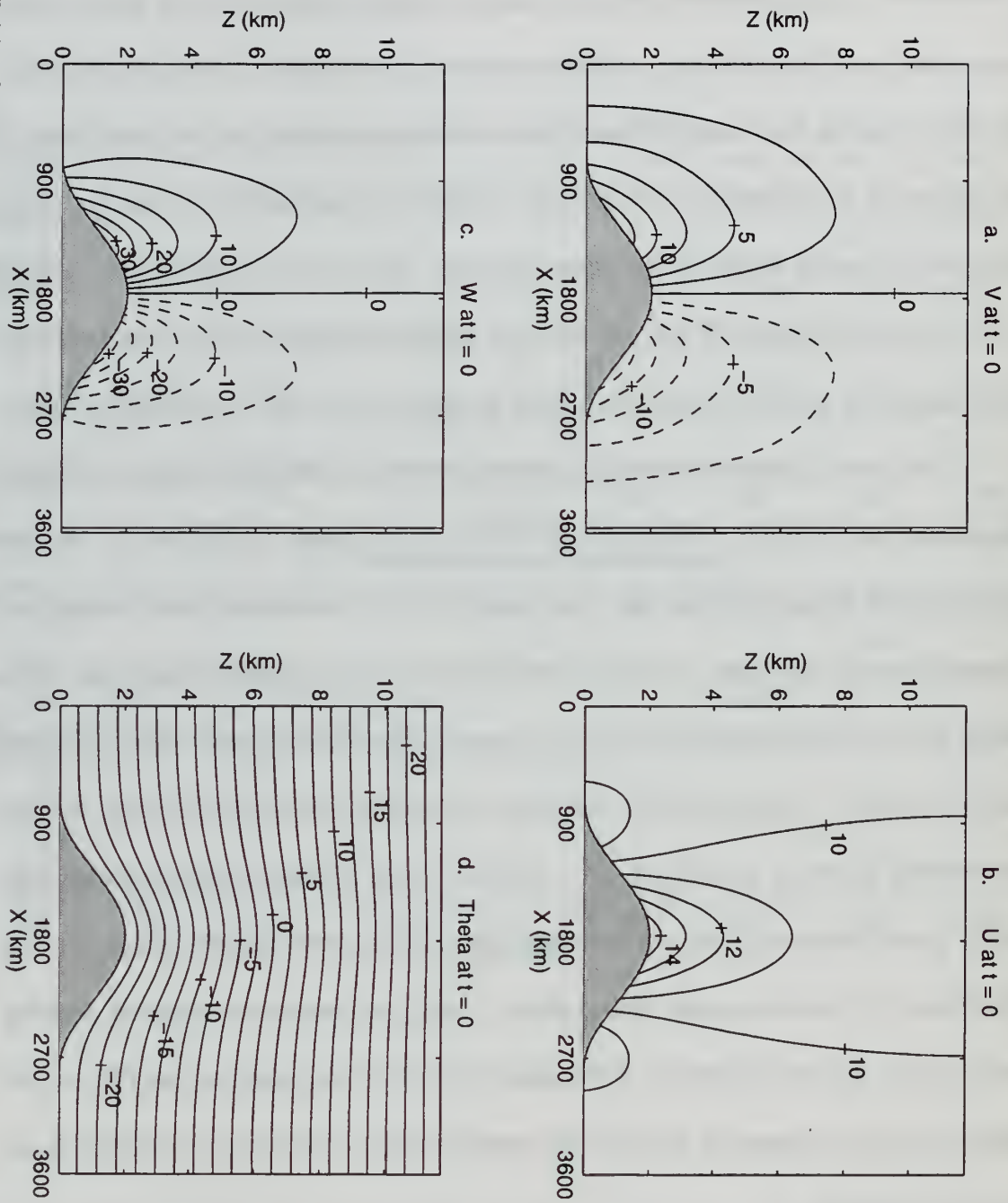
**Figure 4.** Frontal strength parameter for flat topography; solid line: inviscid case; dashed line: PBL case.



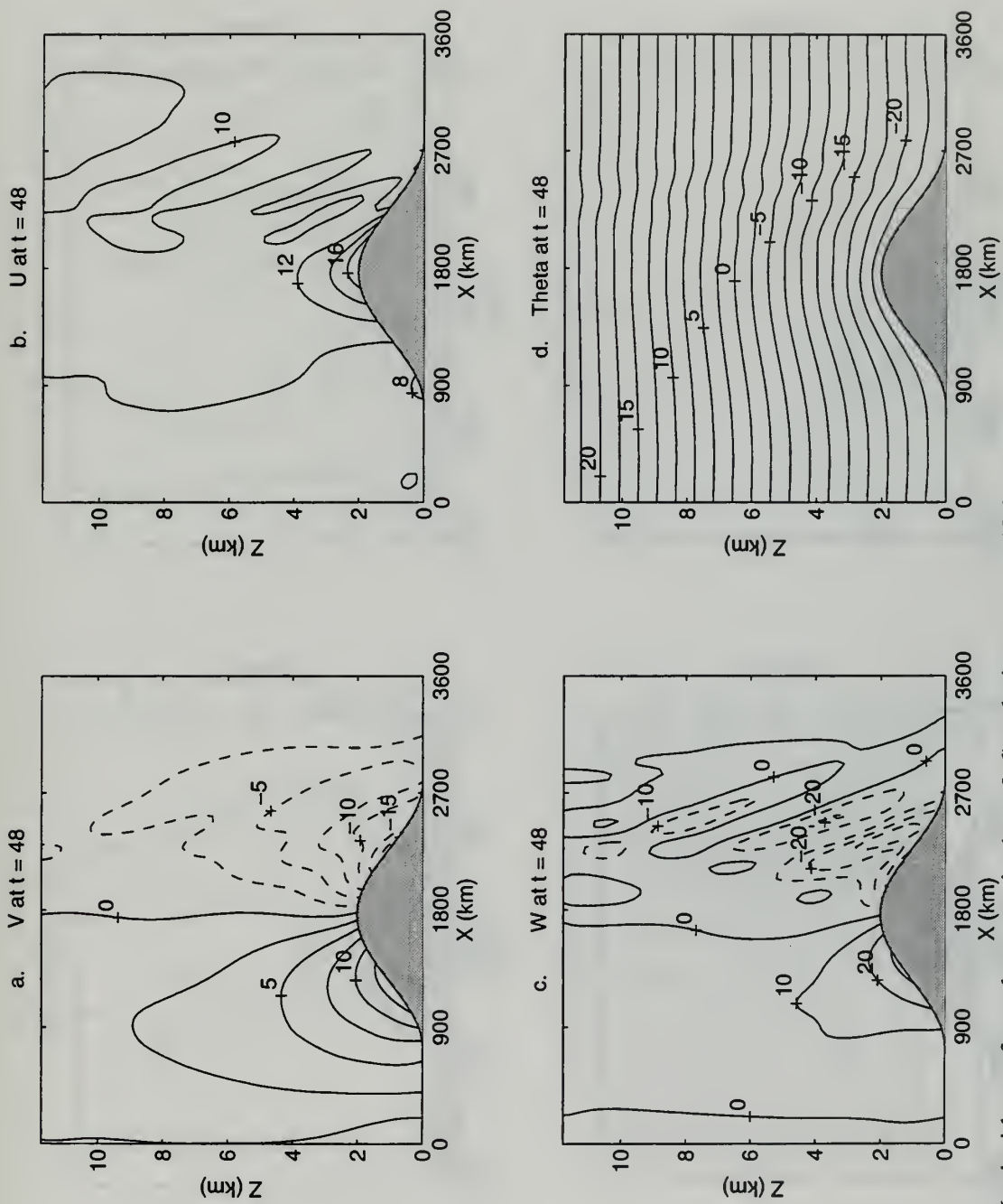
**Figure 5.** Comparison of frontal separation with cross-frontal velocity in flat topography cases: (a) inviscid frontal position minus PBL frontal position, km; (b) maximum cross-frontal velocity, m/s. Solid line: inviscid case; dashed line: PBL case.

Figure 6. The  $w$  contours in Figure 6c are of true vertical velocity in height coordinates. The fields are symmetrical about the ridge axis, as expected. The  $t = 48$  h fields (Figure 7) show only a slight departure from the semigeostrophic solutions as weak wave activity is generated and the cross-ridge velocity maximum shifts slightly toward the lee slope. The PBL solutions for  $t = 48$  h (Figure 8) are more asymmetrical in the lower layers in this respect as the elevated cross-frontal jet is displaced significantly over the lee slope. No gravity waves are evident in the figure, however. The  $\epsilon = 0.4$  ridge produces similar  $t = 48$  h solutions (Figures 9 and 10), but with stronger mountain-forced wind fields and larger amplitude gravity waves, which begin to appear in the PBL case (Figure 10d).

The  $\epsilon = 0.2$  mountain inviscid solution exhibits a dramatic departure from the semigeostrophic solution. The fields at  $t = 48$  h are shown in Figure 11. As the mountain slope becomes steeper, the cross-mountain flow is accelerated more strongly and advected over the lee slope. In the inviscid simulations, the maximum winds are at the surface and an evident hydraulic jump is generated when the high speed winds reach the base of the slope. This causes the well-mixed area at the base of the lee slope and the flow reversal above the lee slope  $u$  and  $v$  maxima. Large amplitude, upward propagating gravity waves also result from the hydraulic jump. In contrast, the PBL solution at  $t = 48$  h (Figure 12) shows no such abrupt effects. Lee slope winds are enhanced, creating gravity waves, but the elevated jet is “insulated” from the topography by the PBL, so the topographic slope changes do not force the abrupt changes in momentum exhibited in the inviscid simulation.



**Figure 6.** Initial fields for non-frontal mountain ( $\epsilon = 0.6$ ) case.



**Figure 7.** Inviscid non-frontal mountain ( $\epsilon = 0.6$ ) solutions at  $t = 48$  h.



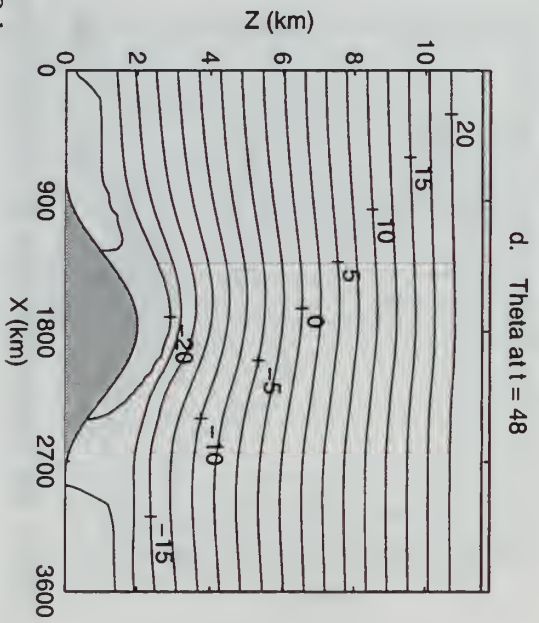
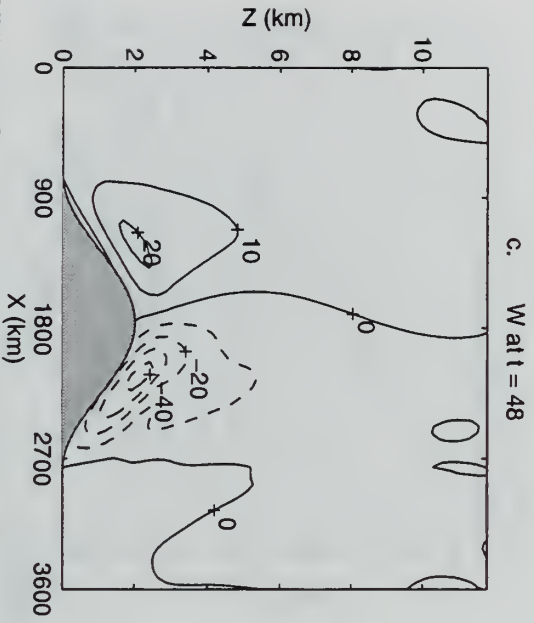
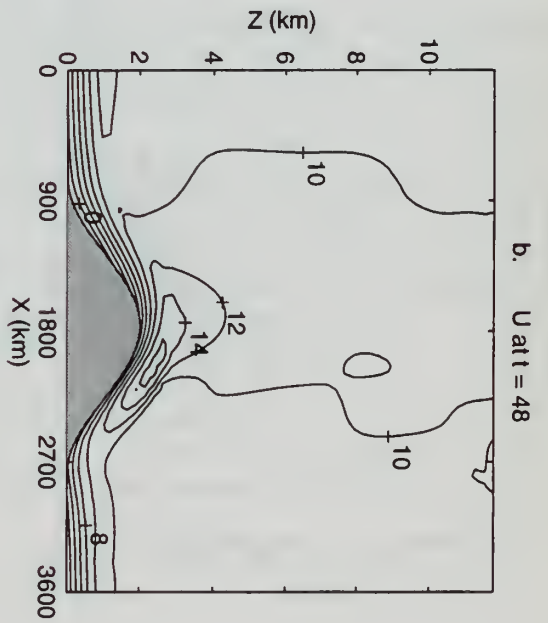
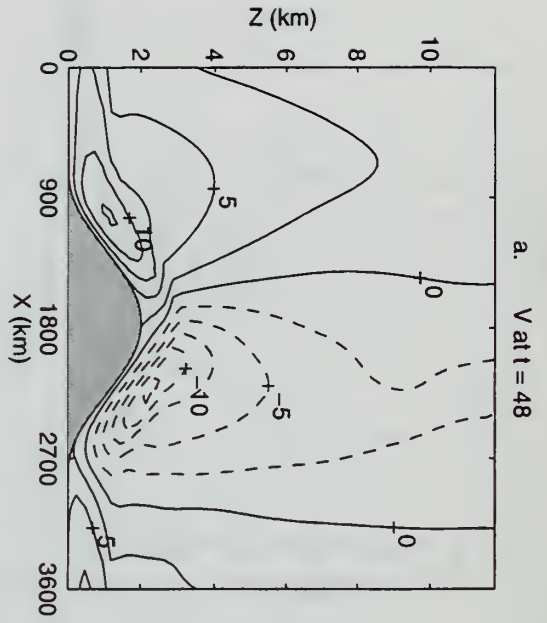
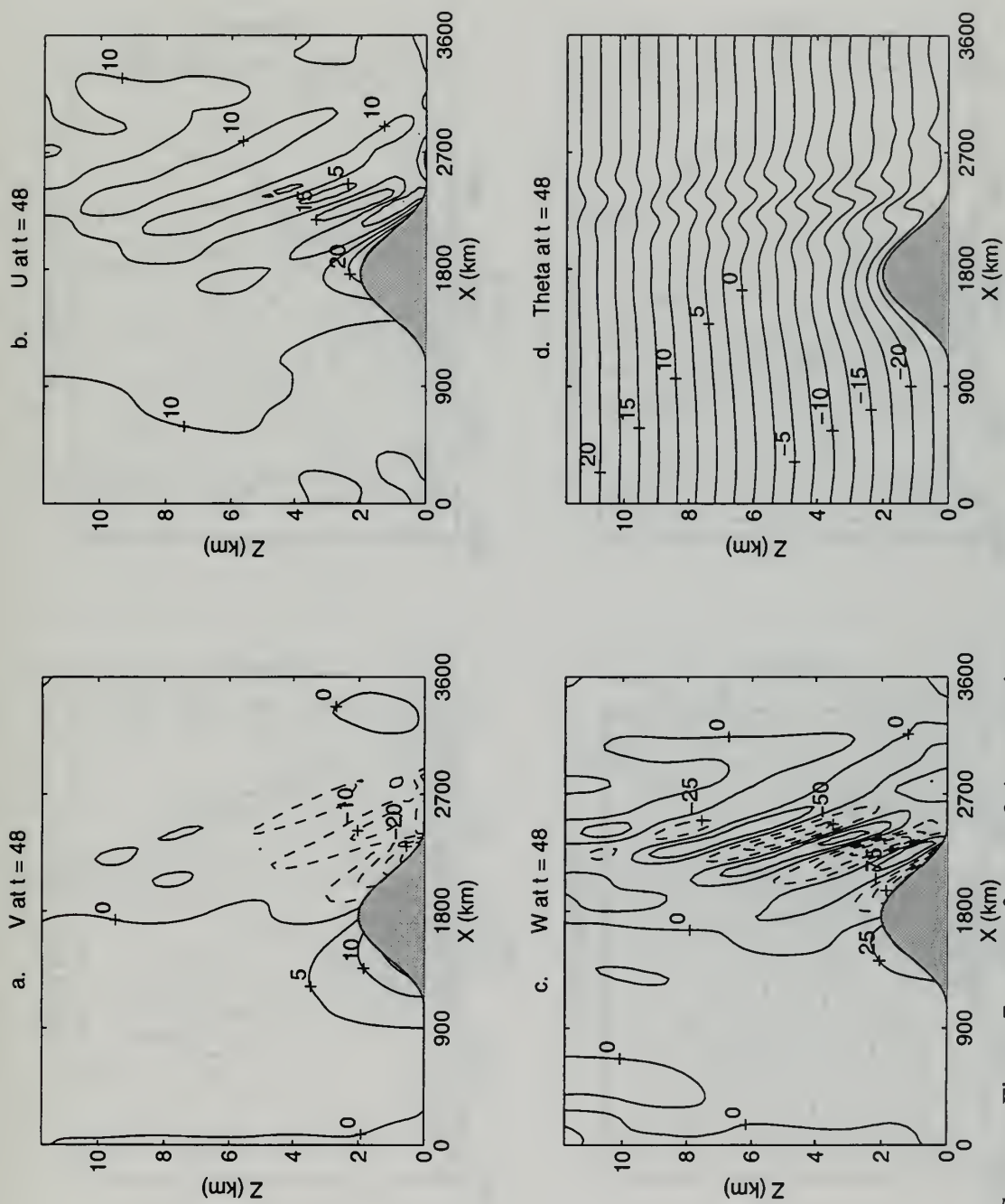
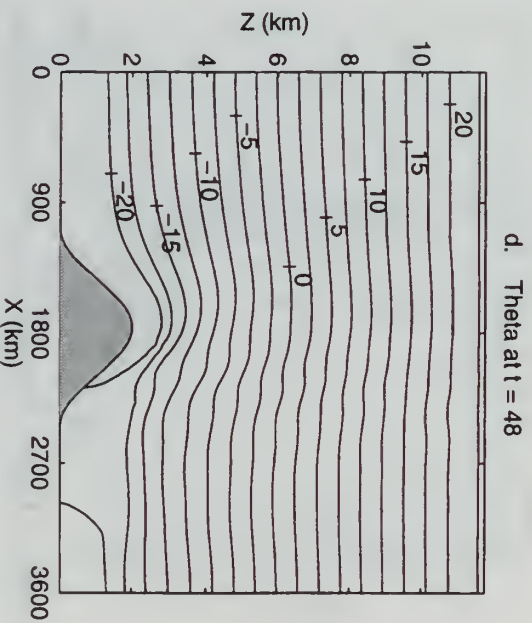
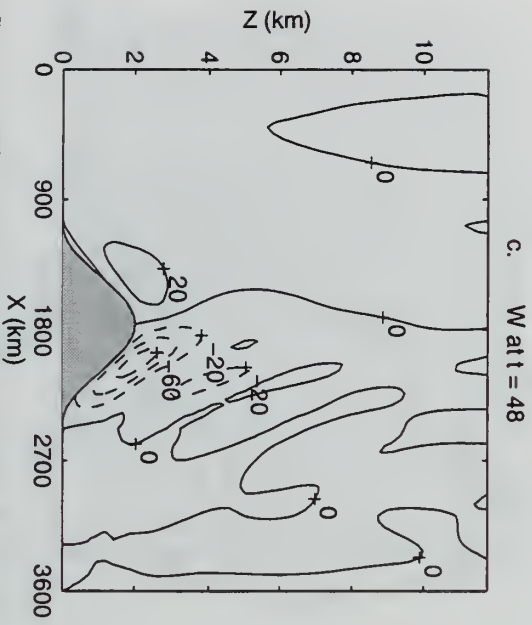
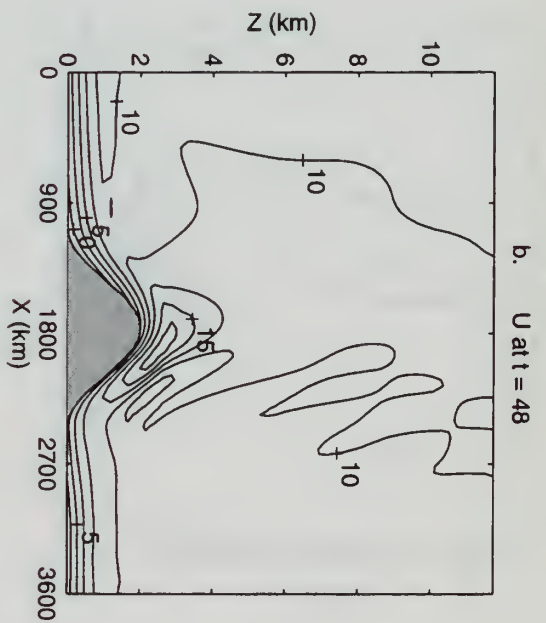
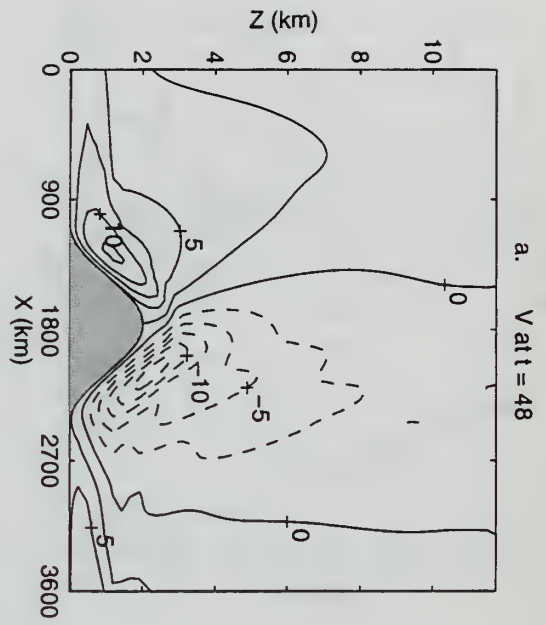


Figure 8. PBL non-frontal mountain ( $\epsilon = 0.6$ ) solutions at  $t = 48$  h.



**Figure 9.** Same as Figure 7 except for  $\epsilon = 0.4$  mountain.



**Figure 10.** Same as Figure 8 except for  $\epsilon = 0.4$  mountain.

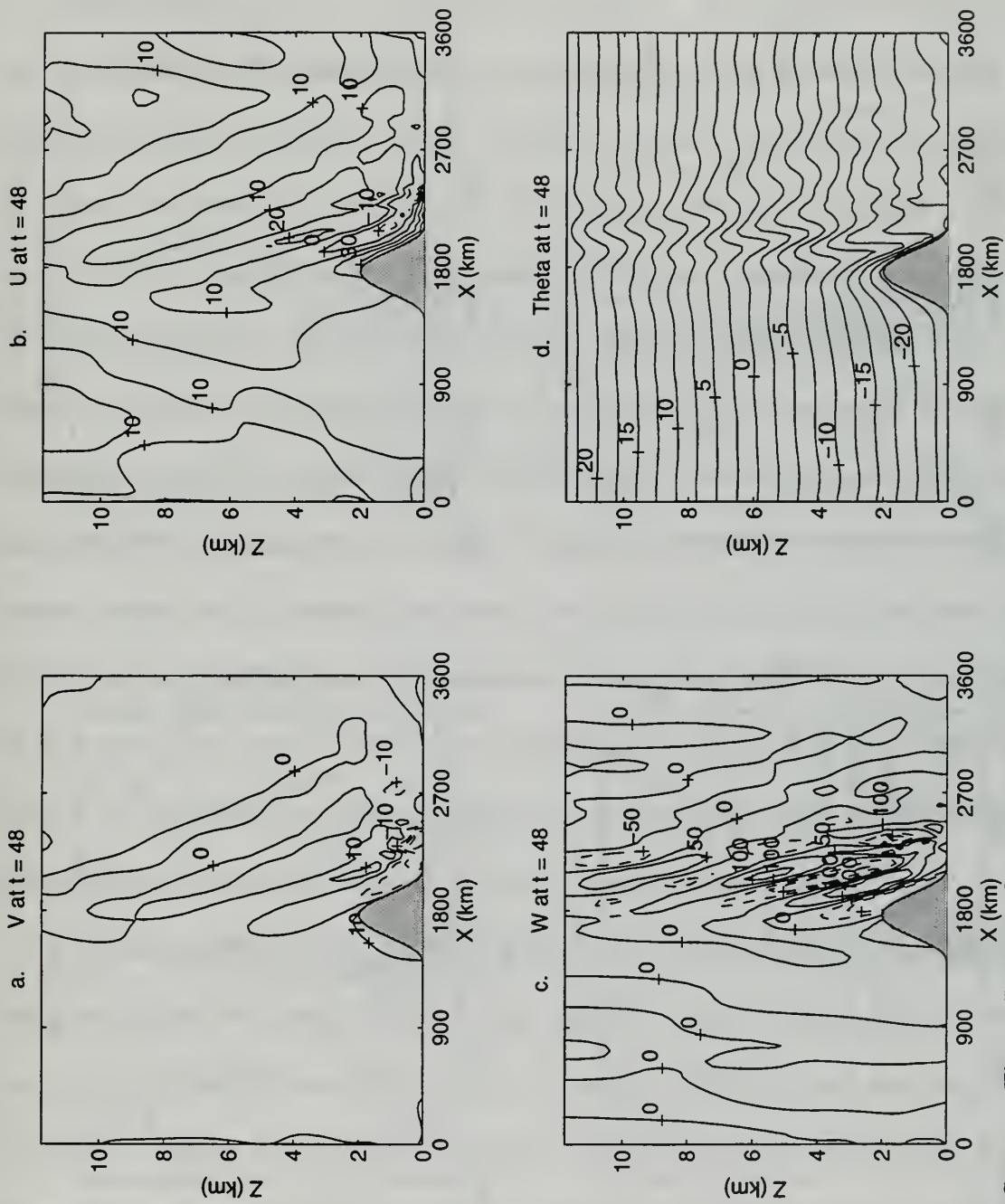


**Figure 11.** Same as Figure 7 except for  $\epsilon = 0.2$  mountain.

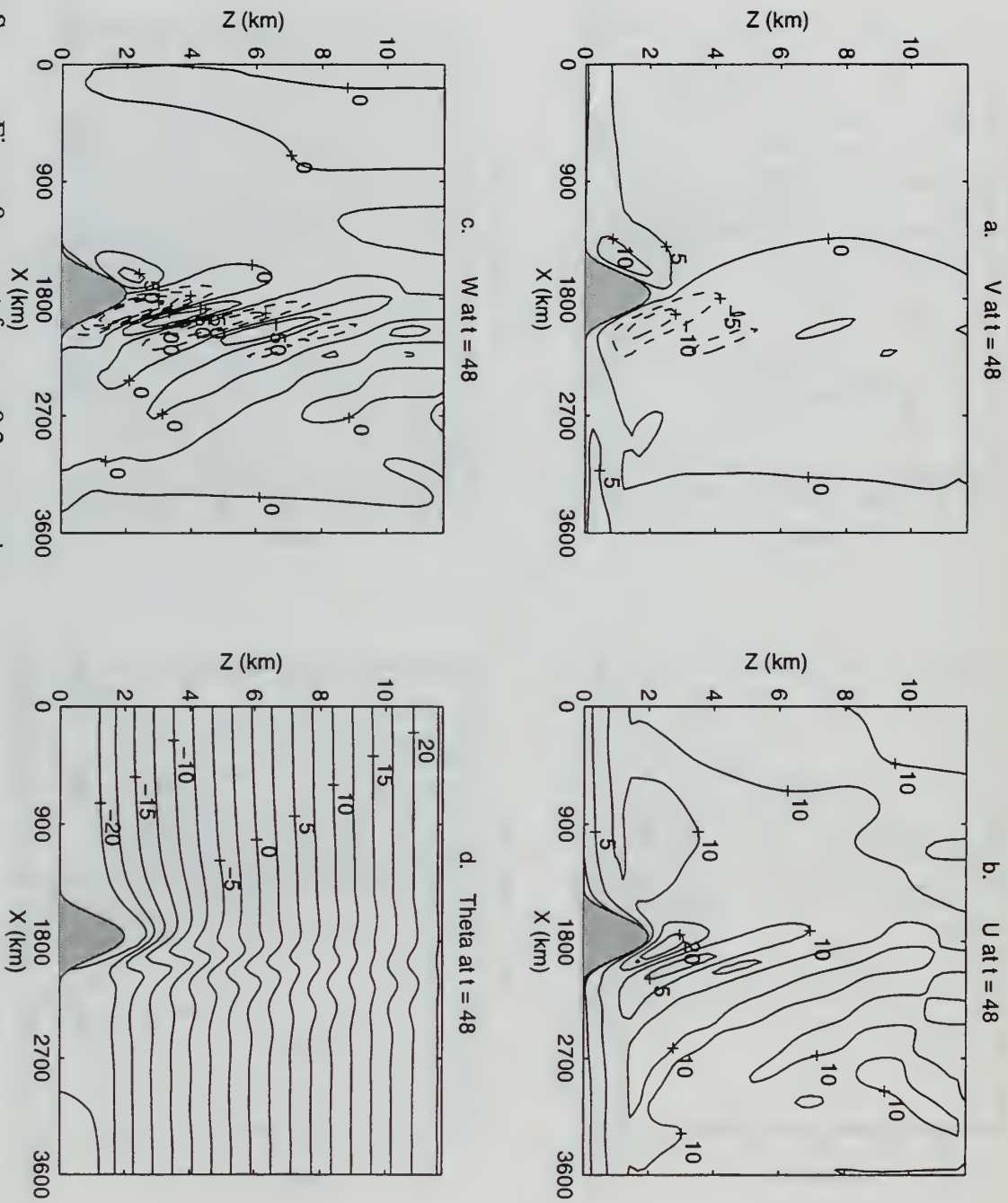


**Figure 12.** Same as Figure 8 except for  $\epsilon = 0.2$  mountain.



In order to investigate the dynamical effects of the mountain-forced circulations on frontogenesis, the divergence fields are examined. The divergence fields of the  $\epsilon = 0.6$  mountain solutions at  $t = 24$  h are shown in Figure 13. The mountain circulations are well-developed by 24 h, and this roughly corresponds to the time that the fronts cross the ridge in the frontal simulations. In the inviscid case (Figure 13a), the flow is divergent on the upwind slope as the air accelerates over the ridge. Strong convergence is shown on the lee slope, caused by the rapid decrease in velocity downstream of the cross-ridge jet velocity maximum. The horizontal divergence field is complicated in the PBL case (Figure 13b) because the wind decreases to zero at the surface, producing significant convergence in the PBL on the upwind slope overridden by a divergent area as the winds above the PBL accelerate over the ridge. This pattern is consistent with the vertical velocity pattern, which increases from zero at the surface to a maximum just above the PBL. Conversely, the lee slope is characterized by divergence within the PBL overridden by an area of convergence. There is less convergence on the lee slope in the PBL case because the winds do not decrease so rapidly near the base. The weaker elevated jet does not enhance the lee side convergence surface as much as in the frictionless case.

The boundary layer also forces a horizontal temperature gradient within the PBL due to vertical mixing on the mountain slope. Vertical mixing reaches a higher  $\theta$ -level near the top of the ridge than near the base because the stability increases over the ridge. The PBL is therefore mixed with air at a higher potential temperature near the top of the ridge. This produces a positive temperature gradient on the upwind slope and a negative temperature gradient on the lee slope, as shown in Figure 14c at  $t = 12$  h. The thermal

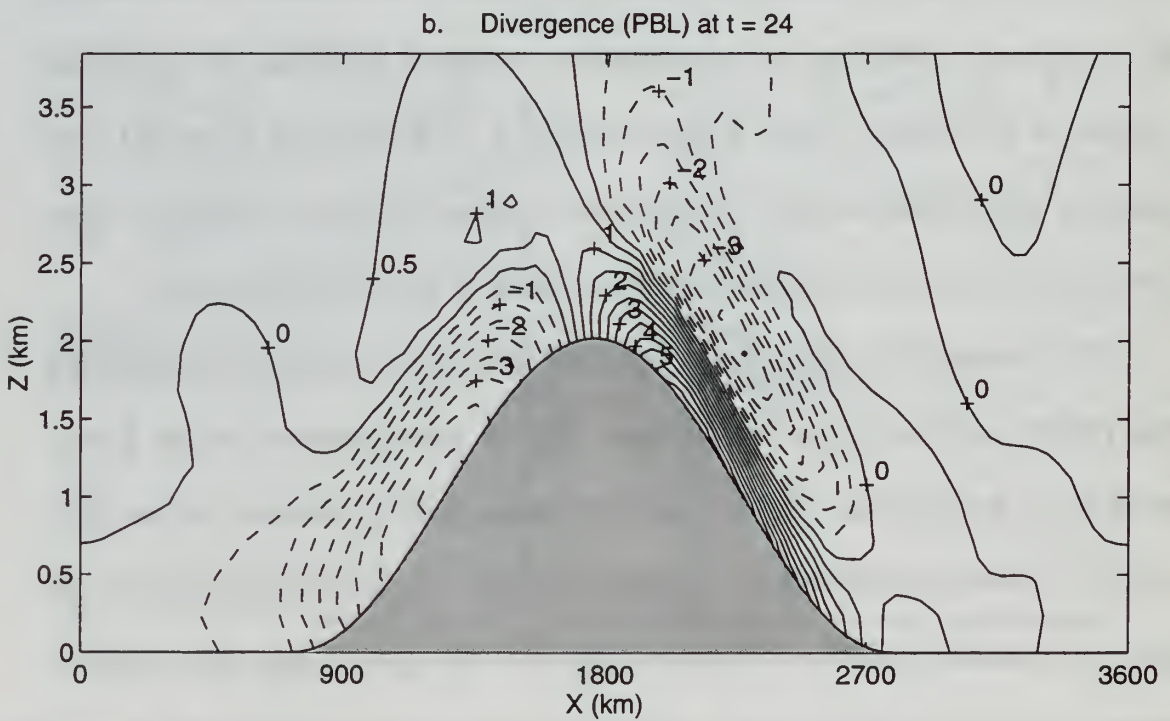
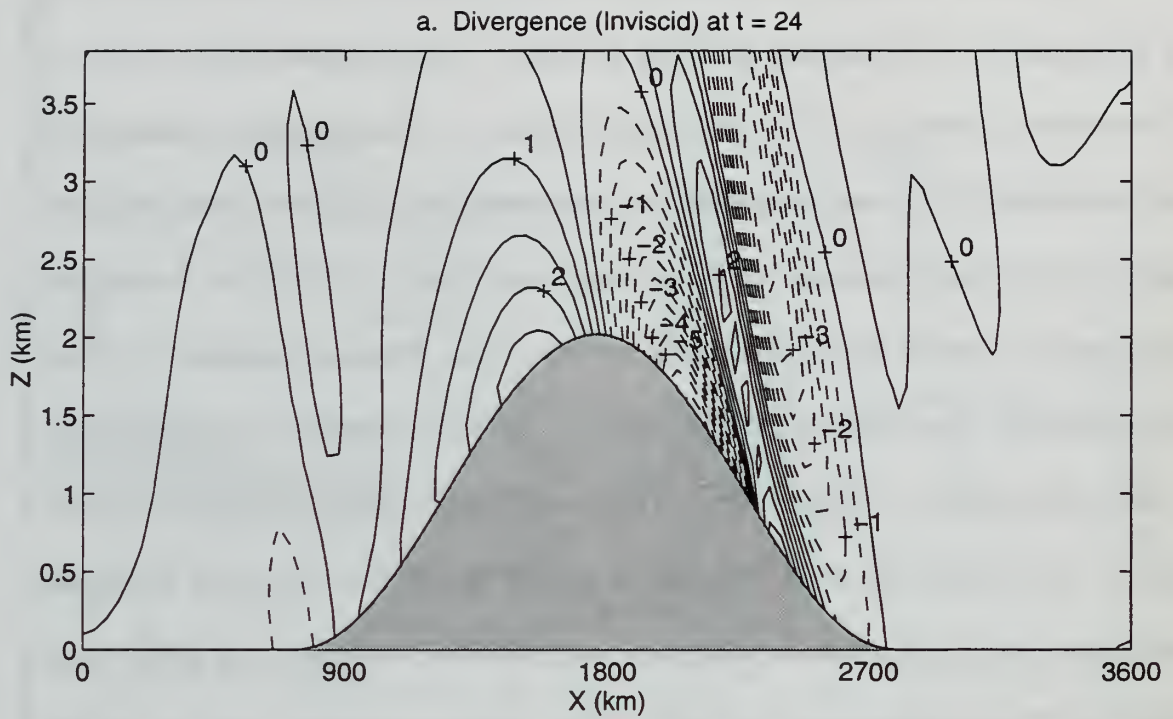


**Figure 13.** Horizontal divergence at  $t = 24$  h for non-frontal mountain ( $\epsilon = 0.6$ ) cases: (a) inviscid case,  $10^{-5} \text{ s}^{-2}$ ; (b) PBL case,  $10^{-5} \text{ s}^{-2}$ .

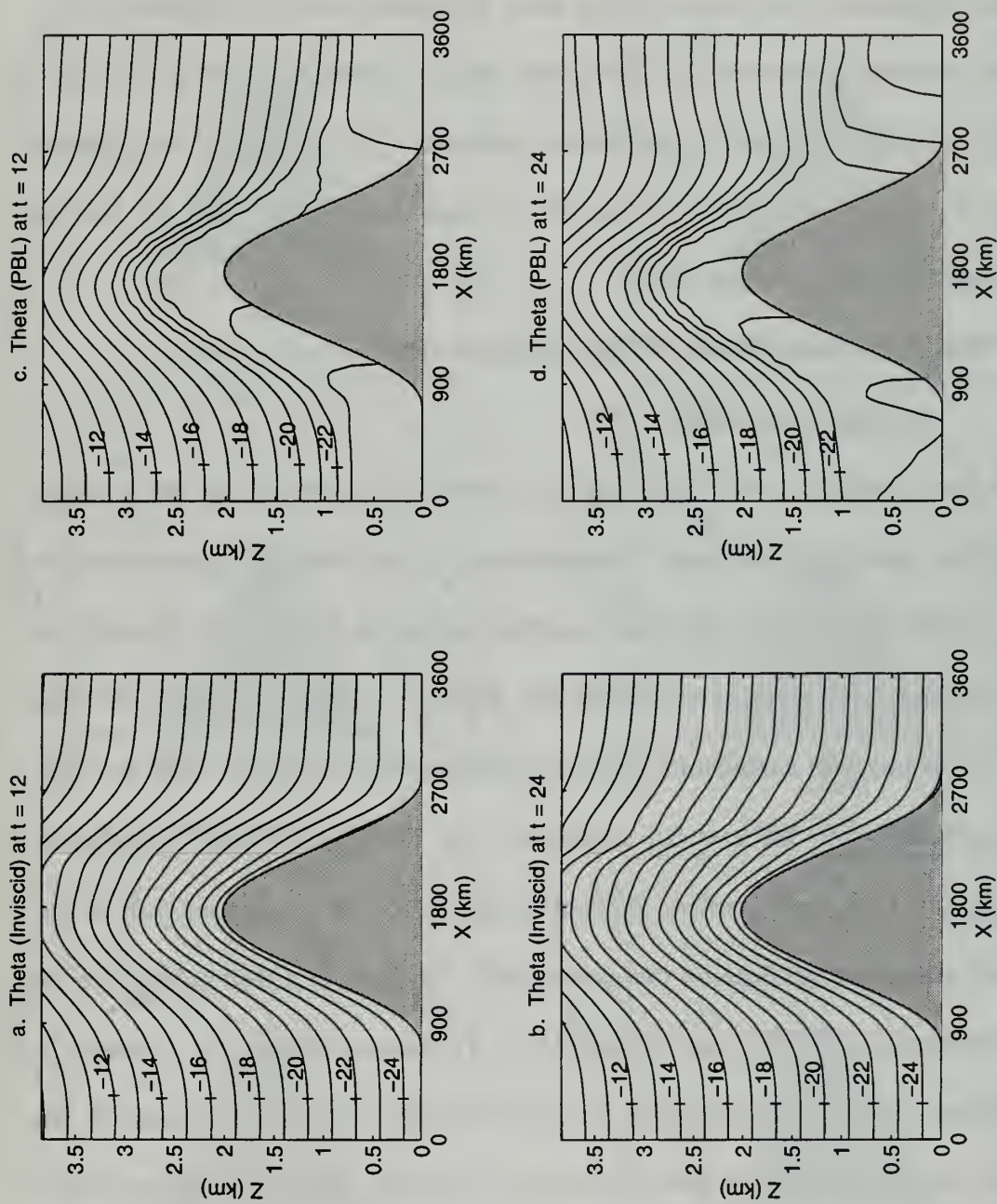


**Figure 14.** Potential temperature fields for non-frontal mountain ( $\epsilon = 0.6$ ) cases: (a) inviscid case at  $t = 12$  h; (b) inviscid case at  $t = 24$  h; (c) PBL case at  $t = 12$  h; (d) PBL case at  $t = 24$  h.



pattern advects downstream somewhat, but is nearly at steady-state by  $t = 24$  h (Figure 14d). The potential temperature fields for the same times in the inviscid case show no significant horizontal temperature gradient along the mountain surface (Figure 14a-b). The effect is unique to the mountain PBL cases because mixing to differing  $\theta$ -levels is required to produce a horizontal temperature gradient. The strength of the gradient produced is also highly dependent on the vertical thermal structure, as will be demonstrated in the frontal simulations.

## C. FRONTAL SOLUTIONS WITH TOPOGRAPHY

### 1. Intensity Variations

In these simulations, the frontal forcing is applied to the model over the mountain domain. The initial conditions are a superposition of the mountain semigeostrophic solutions (Figure 6) and the frontal initial conditions shown in Figure 1. In all cases the axis of the frontal forcing begins at  $x = 900$  km. Figures 15 through 17 contain the time evolution of the potential temperature field at 6 h intervals for both the inviscid and PBL frontal simulations over the  $\epsilon = 0.6$  mountain. The initial temperature perturbation (Figure 15a and 15d) has a positive gradient at the surface on the western half of the domain and a negative gradient on the eastern half. By  $t = 6$  h, a well-mixed layer is already developed in the PBL case (Figure 15e). The vertical mixing has produced a significant strengthening of the surface potential temperature gradient compared to the frictionless potential temperature field (Figure 15b). Here the mixing has a greater effect on the thermal gradient than in the non-frontal case because the initial temperature

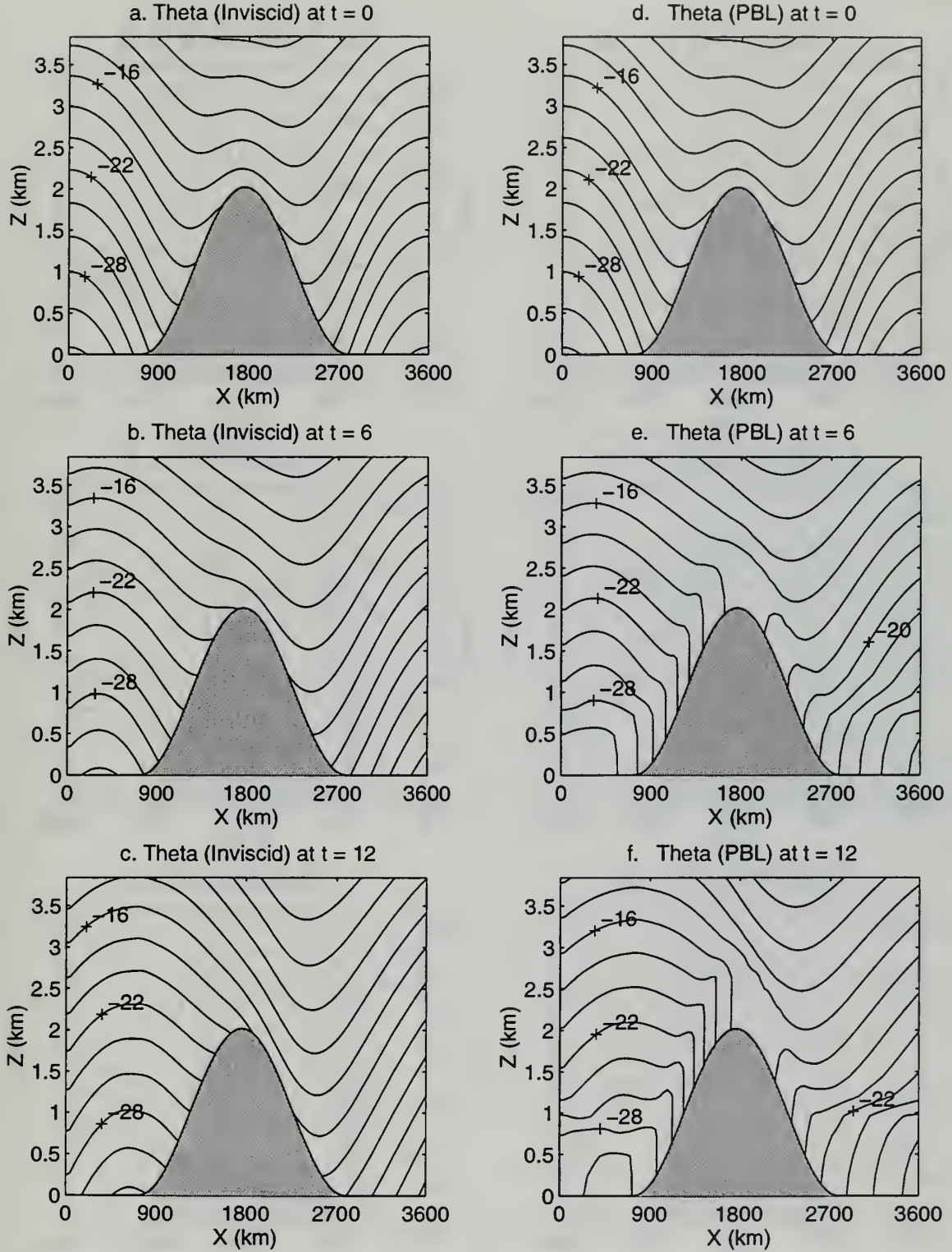


**Figure 15.** Potential temperature fields for frontal mountain ( $\epsilon = 0.6$ ) cases: (a)-(c) inviscid case for  $t = 0$  to  $t = 12$  h; (d)-(f) PBL case for  $t = 0$  to  $t = 12$  h.



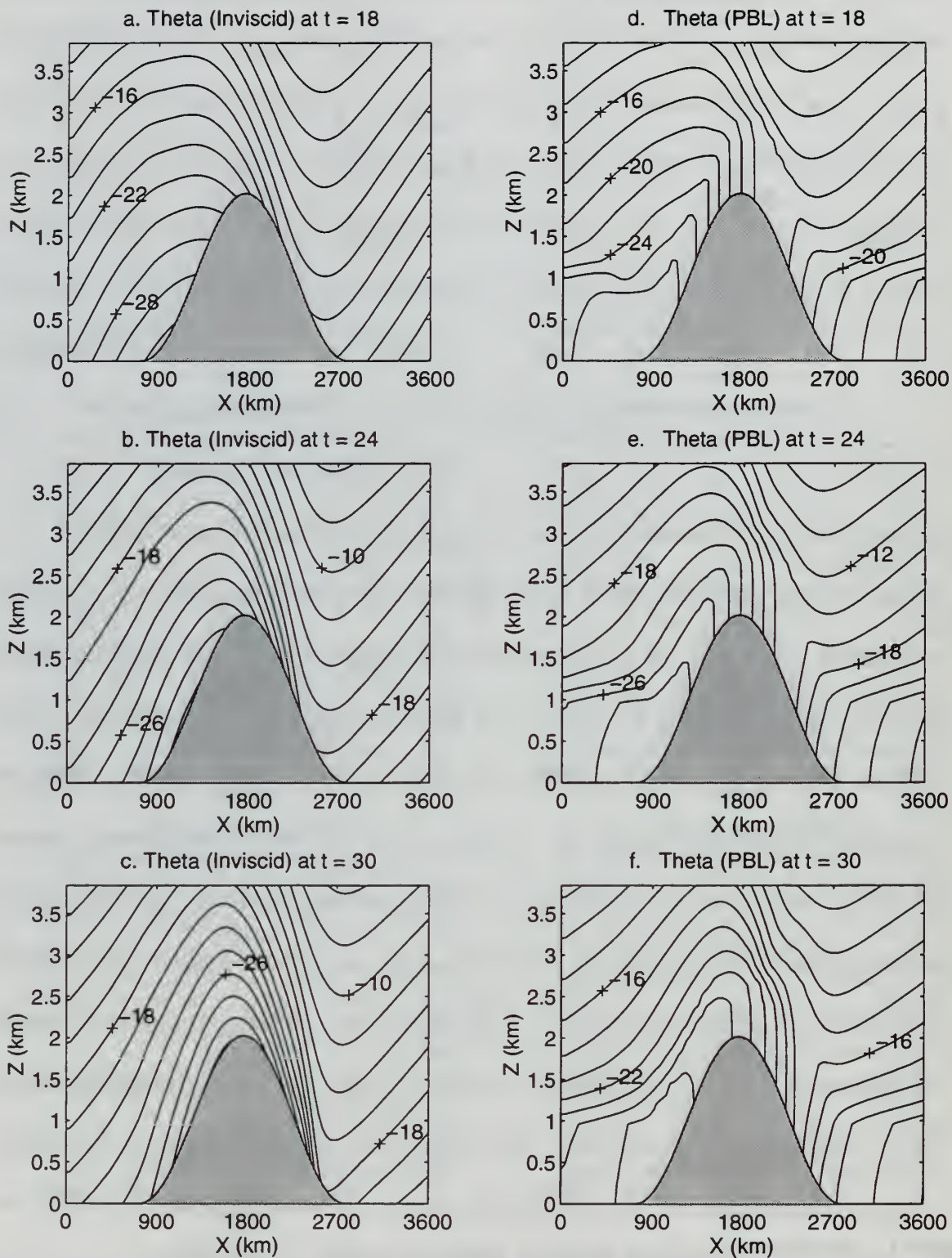


**Figure 16.** Same as Figure 15 except for time  $t = 18$  through  $t = 30$  h.

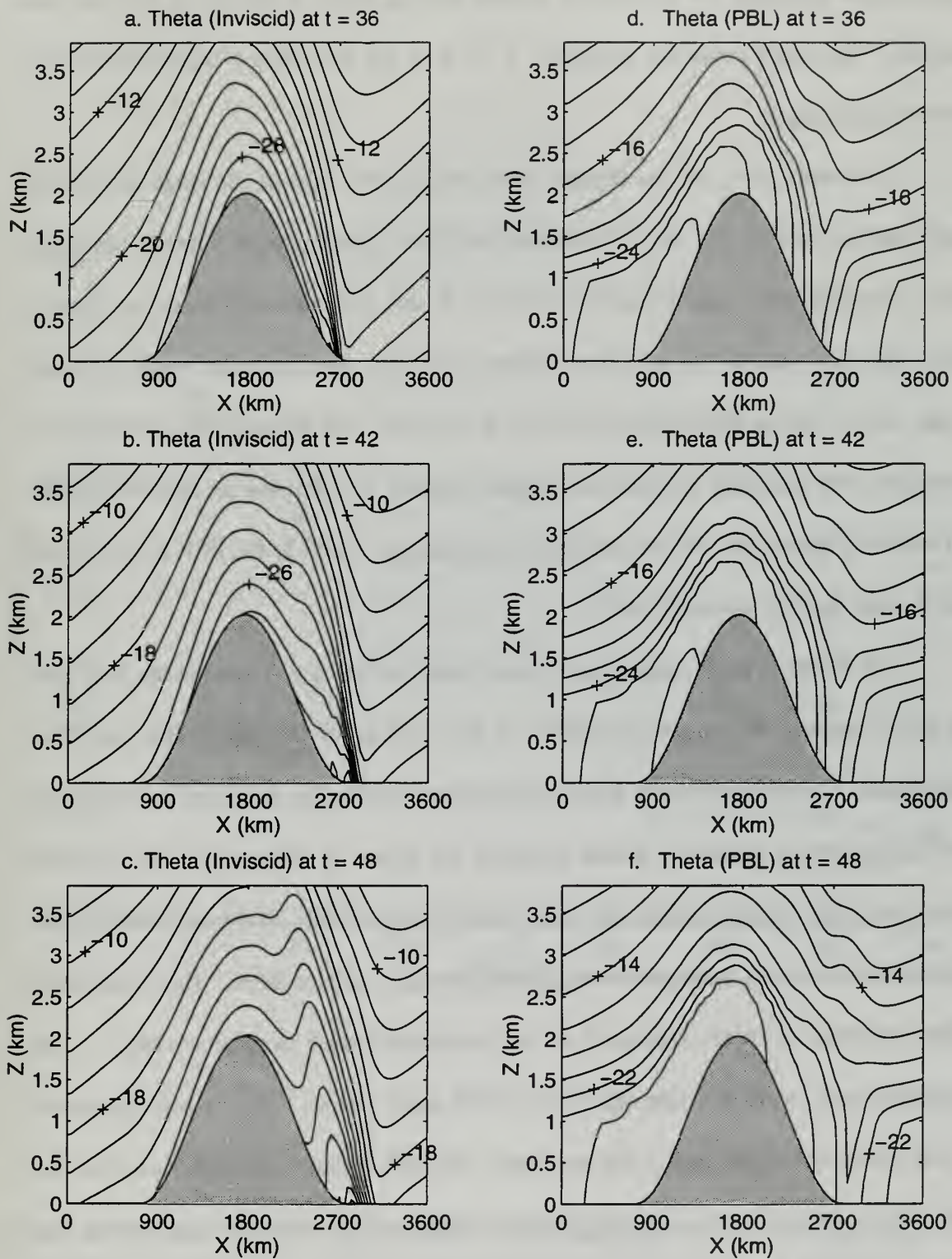


**Figure 17.** Same as Figure 15 except for time  $t = 36$  through  $t = 48$  h.

perturbation increases the differential  $\theta$ -level mixing effect described in the previous section. The trend continues through  $t = 12$  h as the well-mixed layer continues to develop and deepen.

At about  $t = 18$  hr, the inviscid front reaches the crest of the ridge and moves down the lee slope in the next 18 h, undergoing rapid frontogenesis (Figures 16a-c and 17a). The PBL front lags behind by about 12 h, and increases in intensity at a much lower rate as it reaches the lee slope (Figure 16d-f) and then gradually weakens on the lower half of the lee slope (Figure 17d-f). Conversely, the inviscid front continues to strengthen over the entire lee slope and weakens slightly as it reaches the downwind plane at  $t = 48$  h (Figure 17c). By the end of the simulation at  $t = 48$  h, the PBL front is much less intense than the inviscid front.

The frontal strength variations are summarized for the  $\epsilon = 0.6$  mountain in Figure 18, which contains the temporal evolution of the  $d$ -values for both frictionless and PBL simulations. The flat topography frontal solutions are included in the figure for reference. The corresponding six-hourly frontal positions are shown in Figure 19. The  $d$ -values show that in the frictionless case, the front weakens significantly on the upper half of the upwind slope and then undergoes strong frontogenesis on the lee slope. This is the same effect observed in W92, attributed to the mountain-forced divergence field. The weakening near  $t = 48$  h is also observed in W92 and is shown to be caused by a small area of divergence at the base of the lee slope. The PBL  $d$ -value curve confirms that the PBL front is stronger on the upwind slope and weaker on the lee slope compared to the frictionless case.



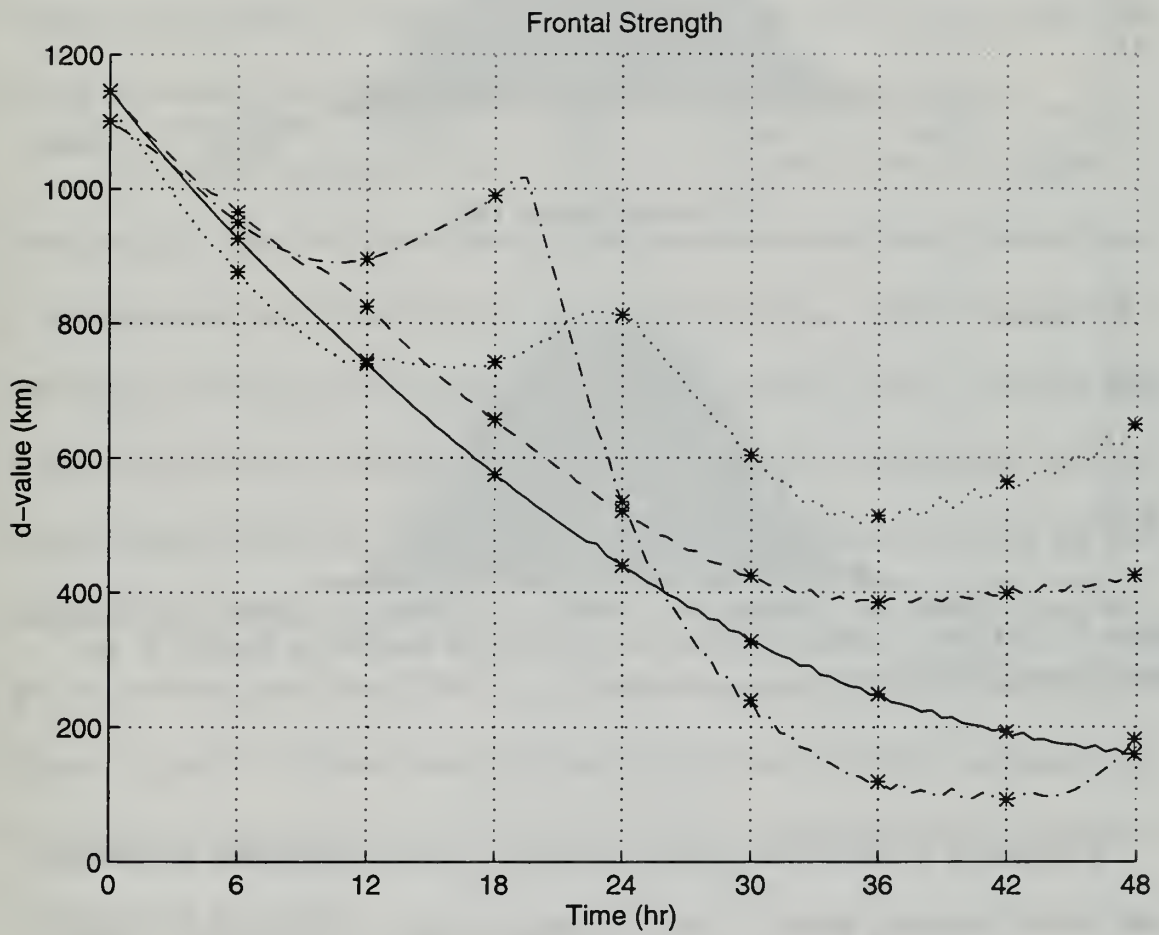


**Figure 18.** Frontal strength parameter for  $\epsilon = 0.6$  mountain; solid line: inviscid flat topography case; dashed line: PBL flat topography case; dot-dashed line: inviscid mountain case; dotted line: PBL mountain case.

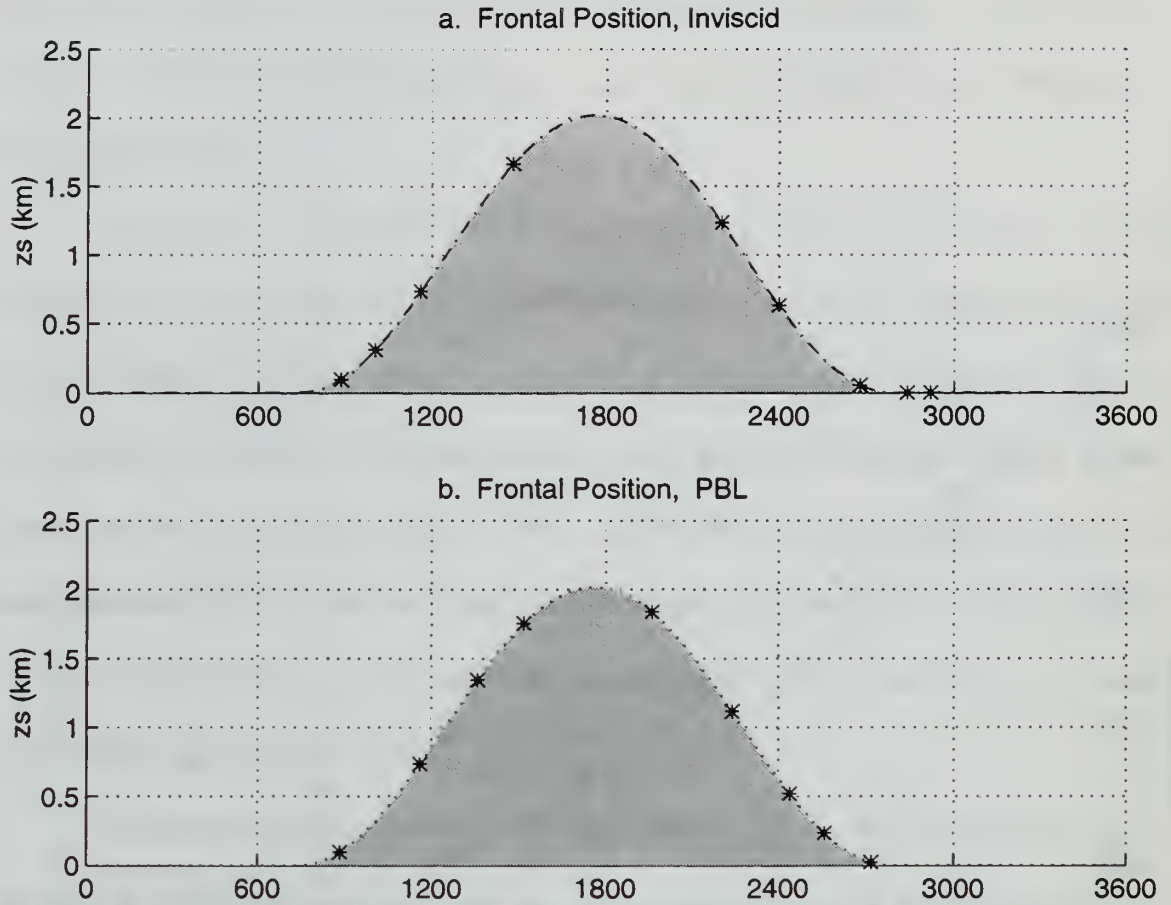


**Figure 19.** Six-hourly frontal positions corresponding to asterisks in Figure 18: (a) inviscid case; (b) PBL case.

Comparison of the  $d$ -value curves to those of the flat topography simulations reveals several interesting features. In the flat topography cases, the PBL front is weaker than the inviscid front at all times. Note also that the inviscid front is weaker in the mountain case than in the flat topography case even on the lower half of the upwind slope (before the period of frontolysis). The mountain PBL front, however, is stronger than both the inviscid mountain front and the flat topography PBL front for the first 12 h of the simulation. Thus the combination of the mountainous topography and the PBL has



a frontogenetical effect on the upwind slope. The overall effect opposes this upwind slope effect, however. The final strength of the fronts in the frictionless simulations are similar whether or not topography is included (confirmed in W92 by extending the integration to  $t = 60$  h). In the PBL simulations, however, the front is significantly weaker in the mountain case at  $t = 48$  h. In contrast to the inviscid results, when PBL effects are included, the mountain appears to have a net frontolytical effect.

The steeper mountain ( $\epsilon = 0.4$ )  $d$ -value plot (Figures 20 and 21) confirms the above analysis. Here the inviscid front is stronger on the upwind slope, but this is due to frontogenesis prior to and right at the base of the ridge. This is caused by a convergence area near the base of the upwind slope (as found in W92). The PBL front is less affected because the PBL effect forces the frontal zone immediately on to the mountain slope (Figure 21). Inspection of the slopes of the curves reveals that the PBL front undergoes greater intensification and less weakening than the inviscid front once they are over the upwind slope. The  $\epsilon = 0.2$  mountain simulation produces similar trends (Figures 22 and 23). Detailed analysis of the mountain-forced intensity variations is not possible with six-hourly time resolution in this case because the fronts move over the bulk of the ridge in 6 h or less.

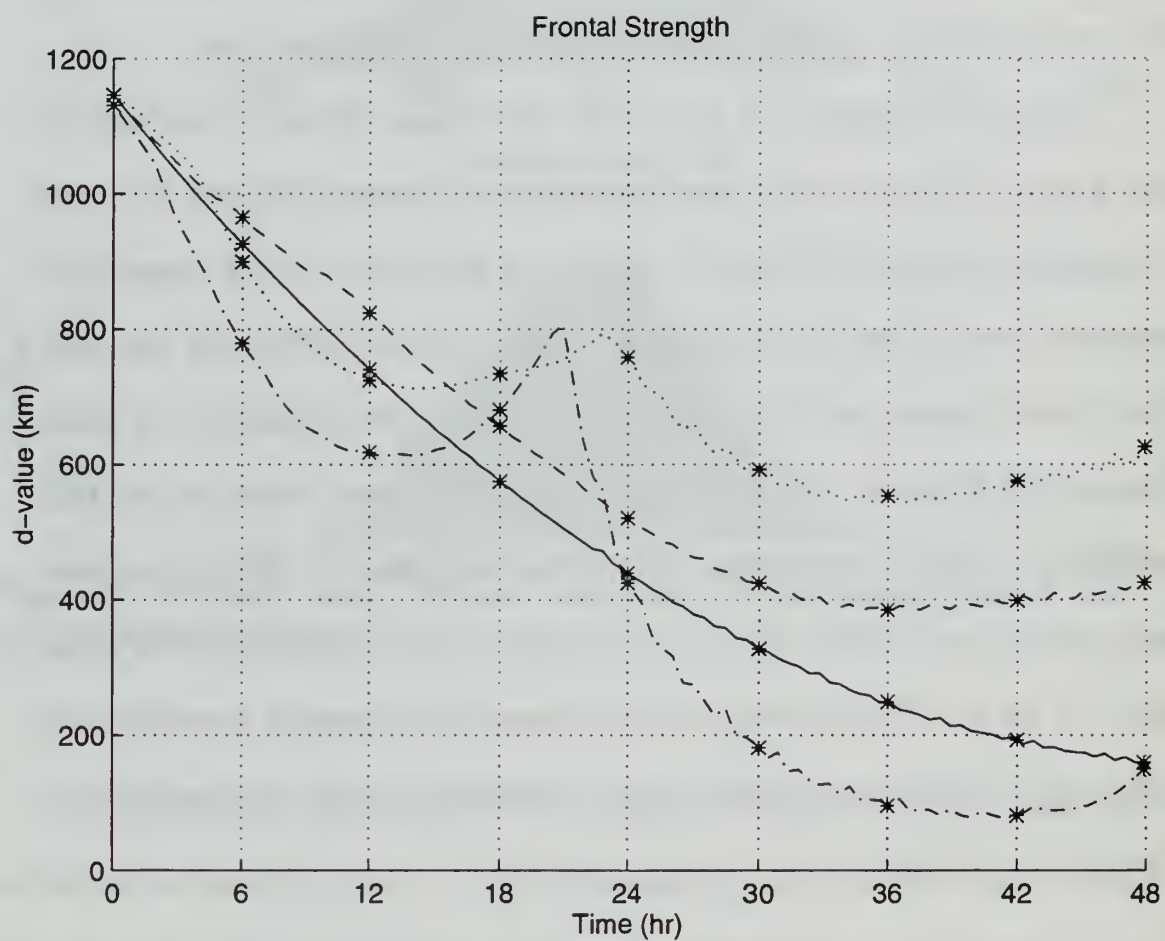
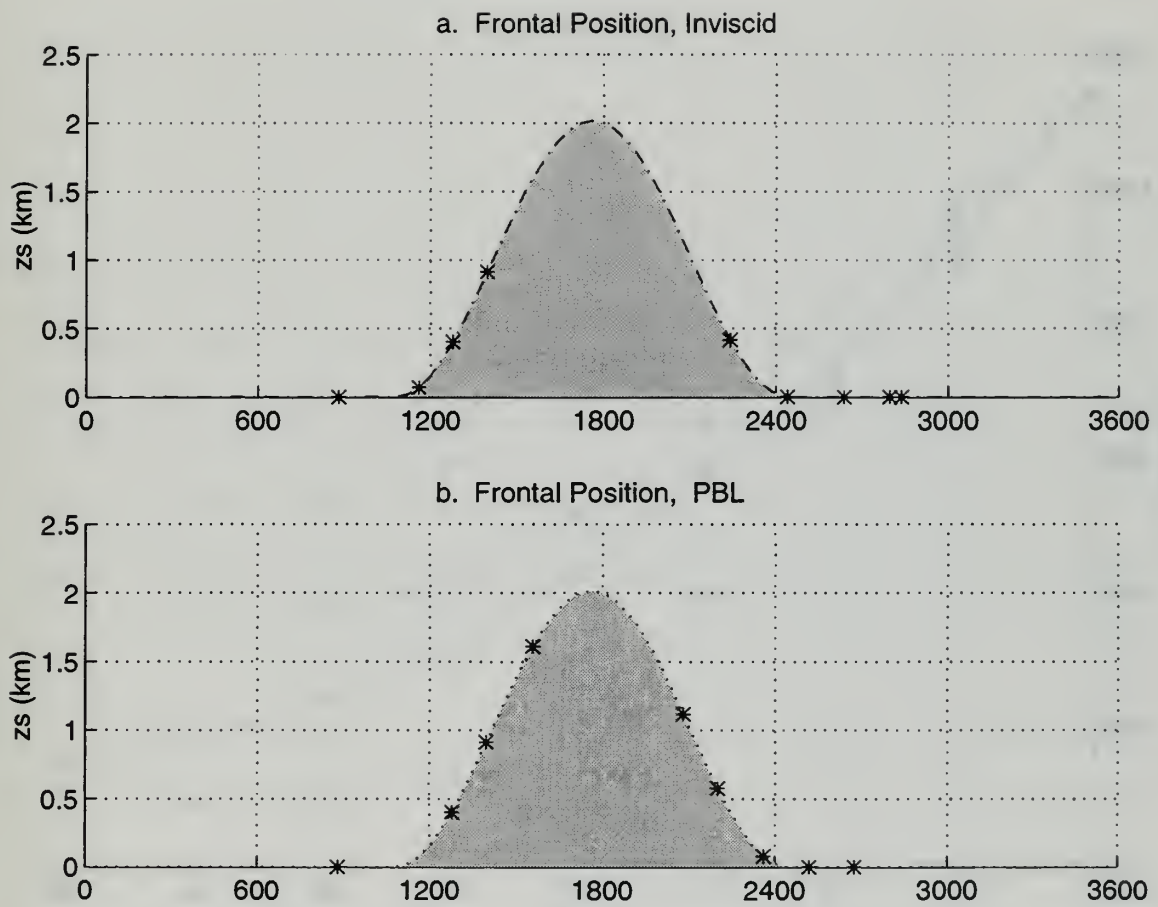


Figure 20. Same as Figure 18 except for  $\epsilon = 0.4$  mountain.



**Figure 21.** Same as Figure 19 except for  $\epsilon = 0.4$  mountain.

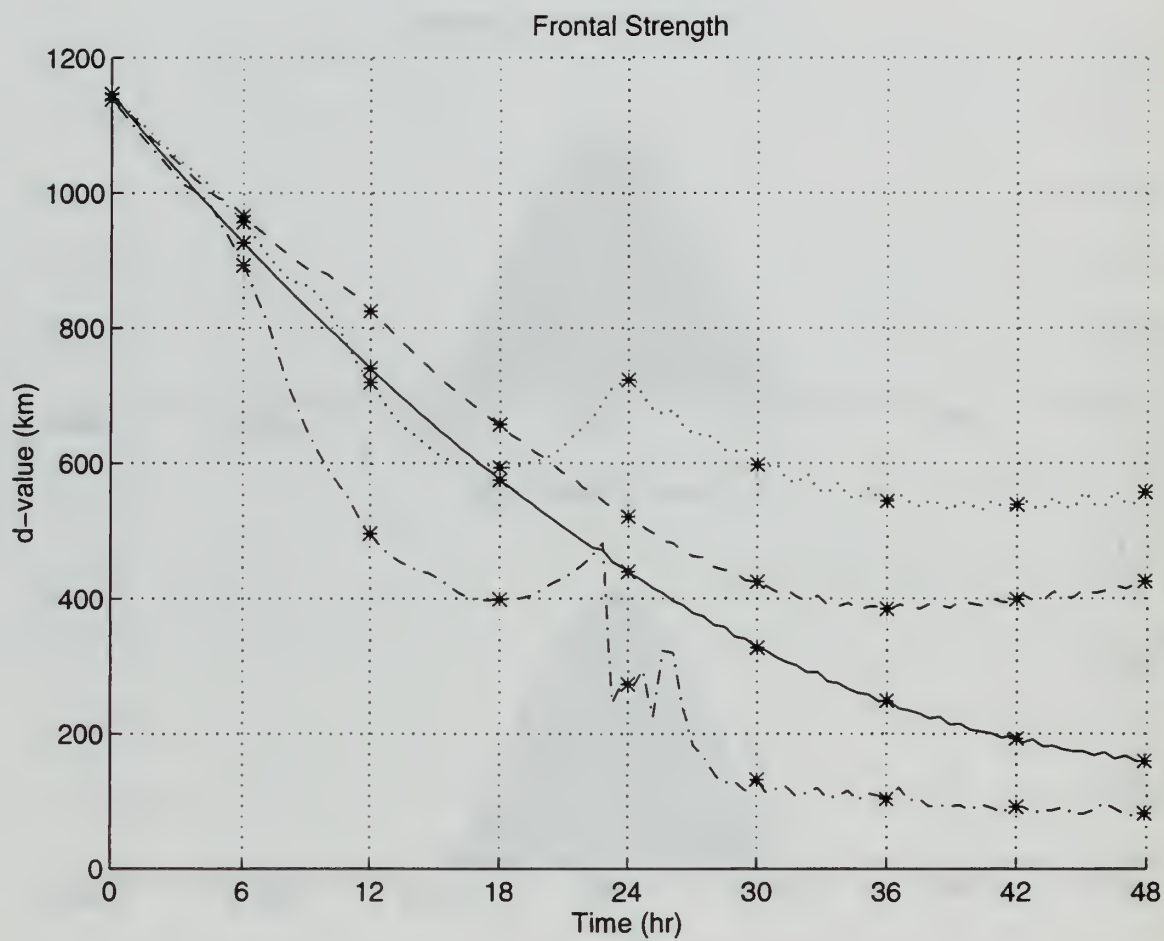
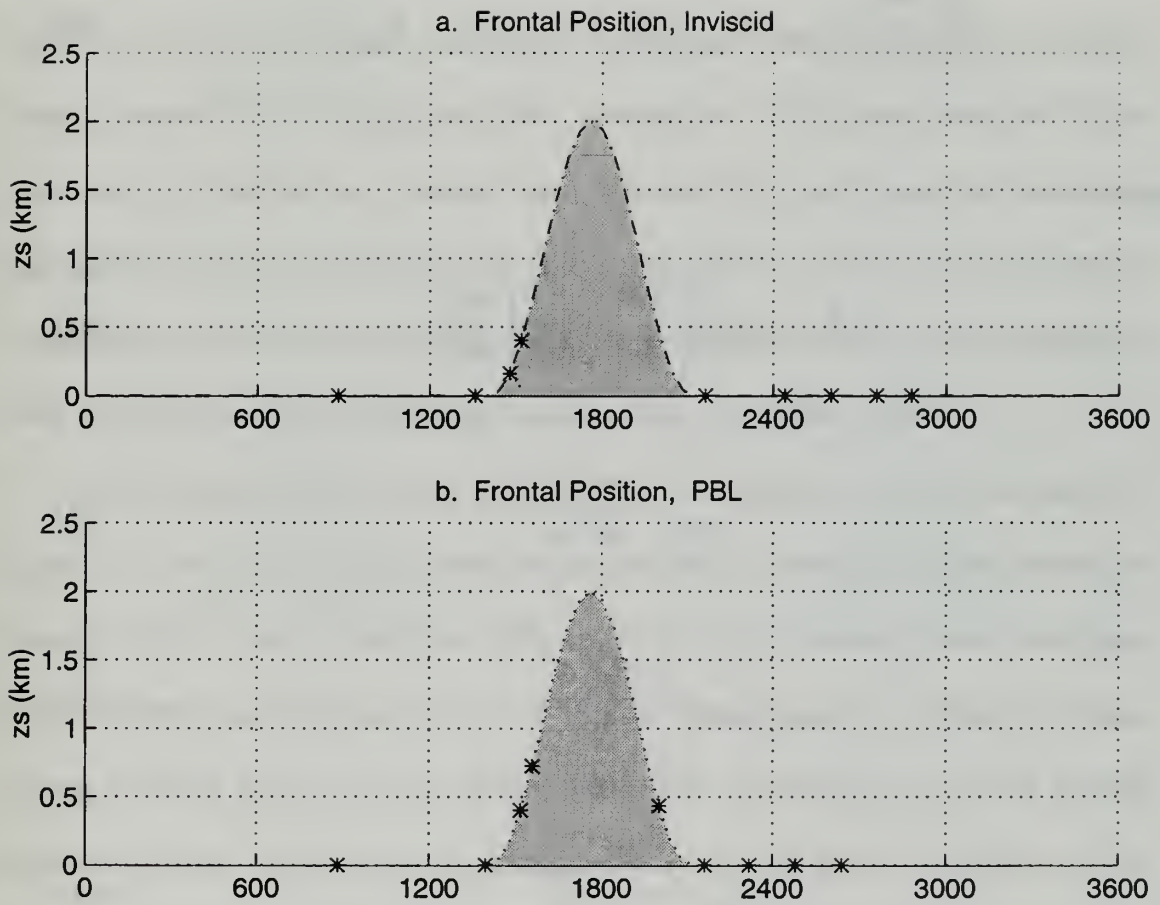


Figure 22. Same as Figure 18 except for  $\epsilon = 0.2$  mountain.



**Figure 23.** Same as Figure 19 except for  $\epsilon = 0.2$  mountain.



## 2. Frontogenetical Forcing

The dynamical mechanisms responsible for the observed variations in frontal intensity can be determined by examining the terms of the frontogenetical forcing function, which can be written as

$$\frac{\partial}{\partial t} \left( \frac{\partial \theta}{\partial x} \right) = F_{adv} + F_{conv} + F_{tilt} + F_{def} + F_{PBL} + F_{diff} + F_{ca} \quad (40)$$

where

$$F_{adv} = -u \frac{\partial}{\partial x} \left( \frac{\partial \theta}{\partial x} \right) - w \frac{\partial}{\partial z} \left( \frac{\partial \theta}{\partial x} \right), \quad (41)$$

$$F_{conv} = -\frac{\partial u}{\partial x} \frac{\partial \theta}{\partial x}, \quad (42)$$

$$F_{tilt} = -\frac{\partial w}{\partial x} \frac{\partial \theta}{\partial z}, \quad (43)$$

$$F_{def} = -\frac{\partial U_d}{\partial x} \frac{\partial \theta}{\partial x}, \quad (44)$$

$$F_{PBL,diff,ca} = -\frac{\partial}{\partial x} \left( \frac{\partial \theta}{\partial t} \right)_{PBL,diff,ca}. \quad (45)$$

The convergence term (equation (42)) does not include the confluence of the deformation field, which is given by the deformation term (equation (44)). The form of equation (45) is from KA82. The terms represented include forcing due to PBL, numerical fourth-order diffusion, and convective adjustment diffusive processes. These terms are not calculated, so a complete summation of forcing terms cannot be computed to explain frontal intensity variations. Rather, the terms  $F_{conv}$ ,  $F_{tilt}$  and  $F_{def}$  are used to determine the differences in forcing between the frictionless and PBL simulations. The figures presented in this section do not include the advective term (equation (41)) and should be considered Lagrangian forcing fields (acting along parcel trajectories). All terms are calculated in  $z$  coordinates and the forcing fields in the figures have been filtered to remove grid-scale noise introduced in the numerical derivatives of the interpolated fields.

The frontogenetical forcing fields for the  $\epsilon = 0.6$  ridge at  $t = 6$  h are shown in Figure 24. The PBL simulation produces relatively large convergence forcing within the boundary layer on the upwind slope (Figure 24d). This is caused by the convergence within the PBL and compounded by the stronger thermal gradient induced by vertical mixing (note the  $\partial\theta/\partial x$  factor in equation (42)). The convergence term in the inviscid simulation shows weak frontolytical forcing (Figure 24a) due to divergence. The compounding effect of the PBL temperature gradient is also observed in the deformation forcing field (Figure 24c and 24f). Here the confluence in the PBL case is equal to that in the inviscid case, so the increased forcing in the PBL case is caused solely by the

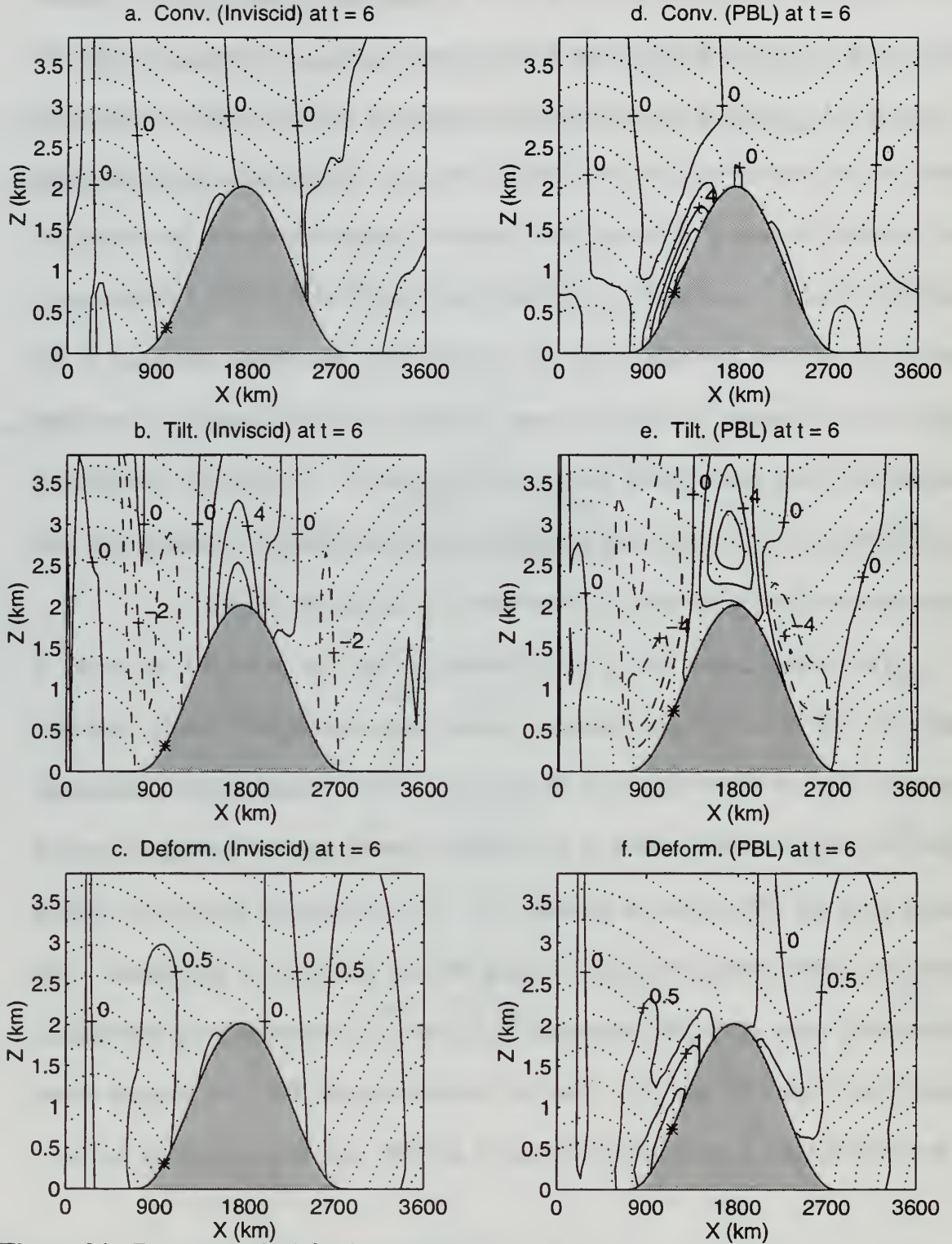


**Figure 24.** Frontogenetical forcing fields at  $t = 6$  h for  $\epsilon = 0.6$  mountain: (a)-(c) inviscid case; (d)-(f) PBL case (all in  $10^{-10}$  deg C  $m^{-1} s^{-1}$ ). Dotted lines are potential temperature contours; an asterisk indicates the location of the surface front.

greater temperature gradient within the PBL. The tilting term is frontolytical in both cases (Figure 24b and 24e) on the upwind slope and is larger in the PBL simulation, partially offsetting the increased convergence forcing.

Figure 25 contains the forcing fields at  $t = 18$  h, when the fronts are near the crest of the ridge. The inviscid front is weakening because of the negative convergence and tilting forcing upwind of the ridge crest. At the top of the ridge, the tilting term is strongly frontogenetic and dominates the convergence forcing (Figure 25a-b). The PBL smoothes the transition from upward to downward vertical motion at the crest (reduces  $\partial w / \partial x$  in equation (43)) and produces a weaker tilting effect. Forcing is nearly balanced at the PBL front as indicated by the neutral trend at  $t = 18$  h in Figure 18. Convergence forcing is still positive but weakening near the crest of the ridge, and tilting forcing is much weaker than in the inviscid case (Figure 25d-e). The tilting term is positive at all times over the top of the ridge and in fact does not vary much in magnitude as the front moves over the ridge. This suggests that the tilting effect is produced largely by the basic flow over the ridge. The forcing fields for the basic flow at  $t = 18$  h are shown in Figure 26. Comparison of the tilting term field at the top of the ridge shows little difference in the magnitude of the forcing produced by the basic field alone and that of the frontal case.

As the fronts move on to the lee slope (Figure 27, at  $t = 24$  h), the inviscid front enters the strong convergence area producing strong positive convergence forcing. In agreement with Gross (1994), tilting forcing becomes significantly frontolytical as the front passes through the lee side vertical velocity maximum, but in this case the positive



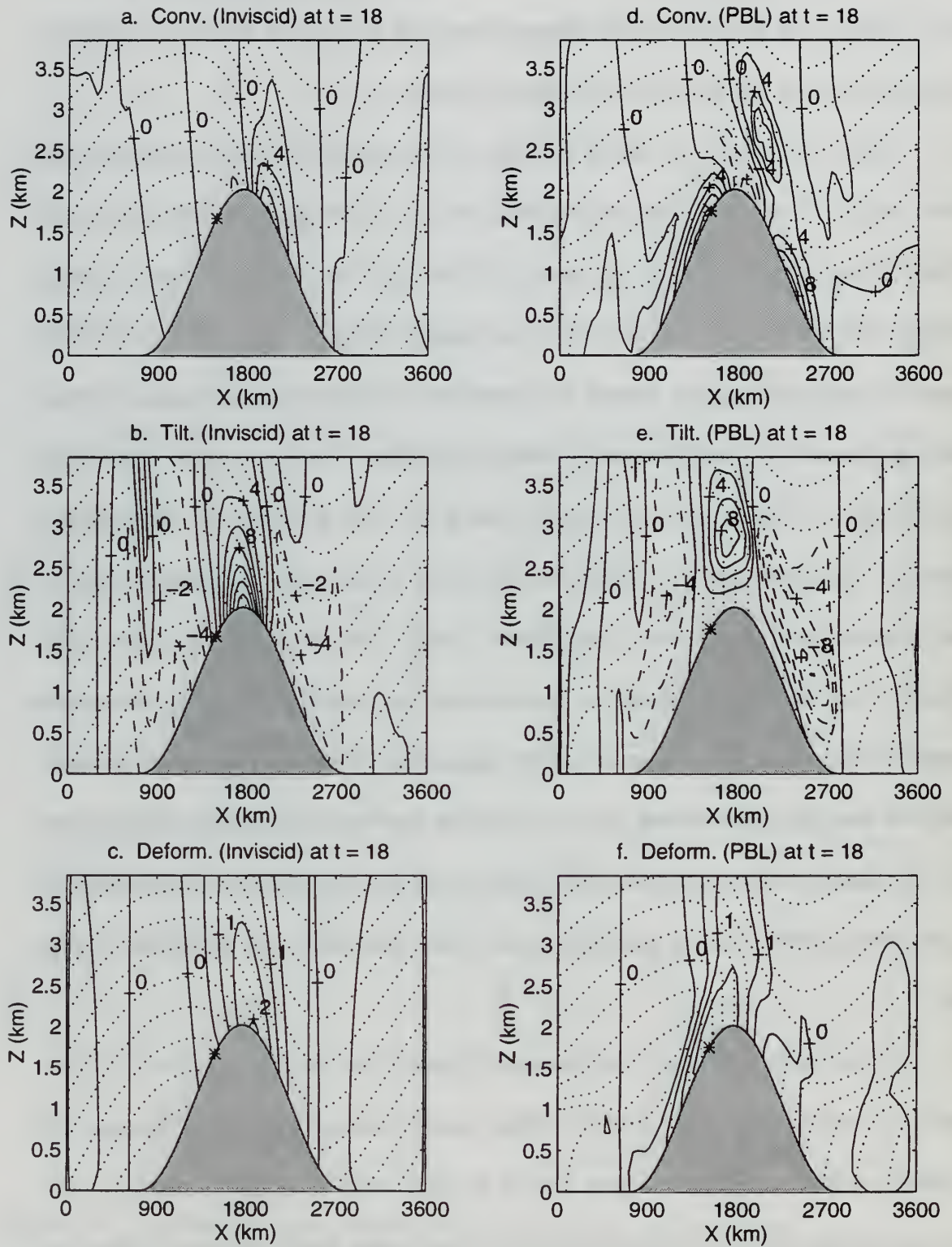


**Figure 25.** Same as Figure 24 except for  $t = 18$  h.



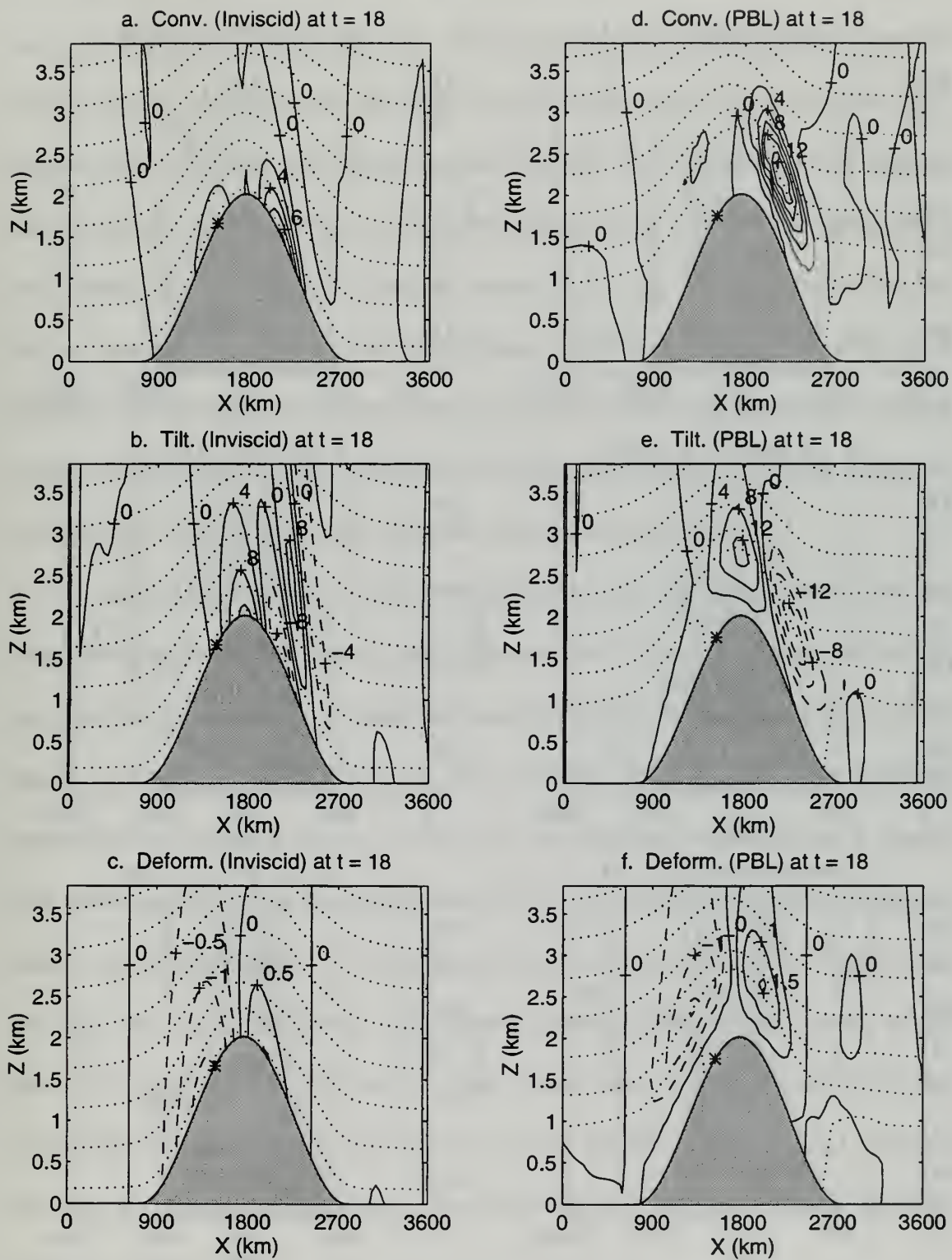


**Figure 26.** Same as Figure 25 except for non-frontal cases.

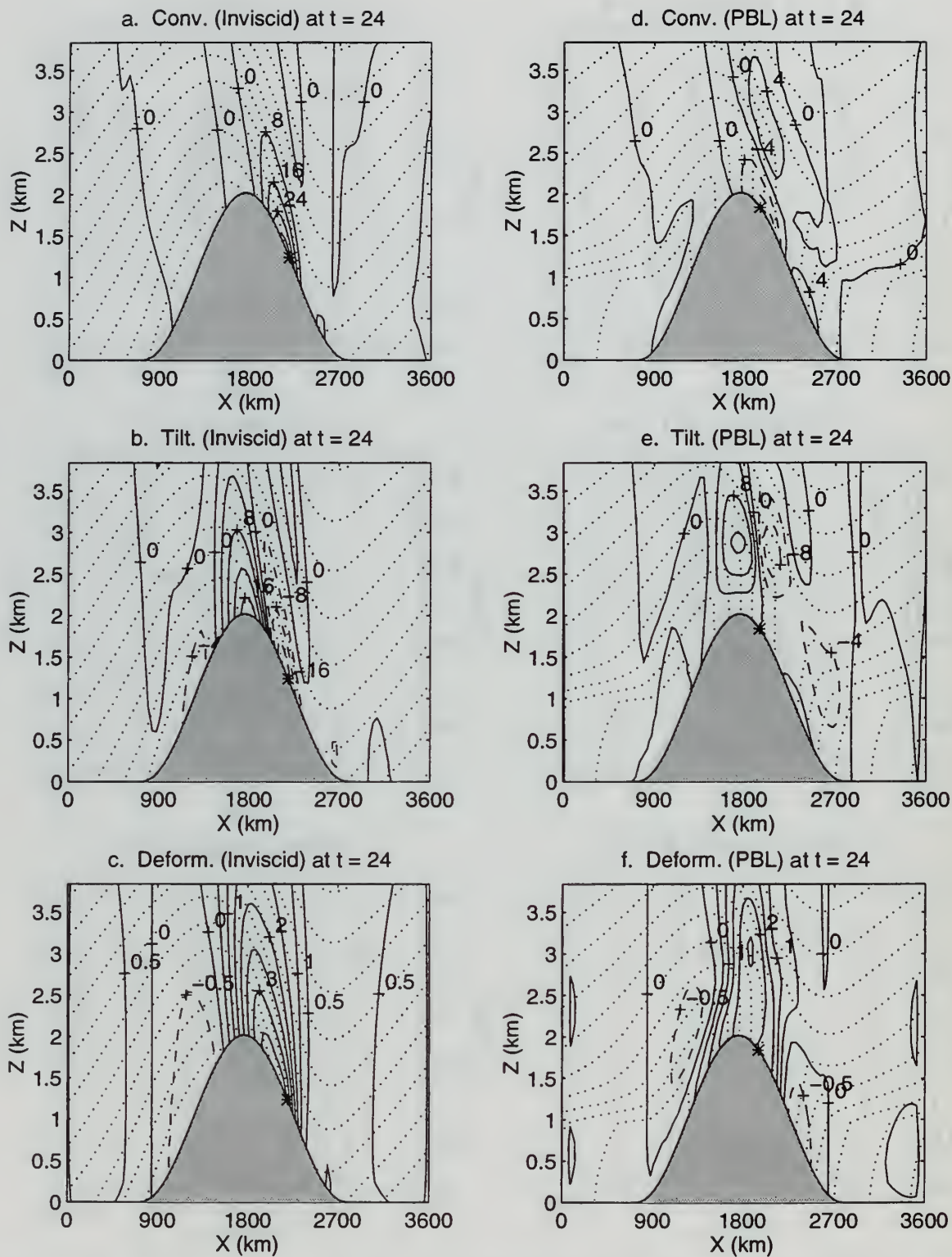


**Figure 27.** Same as Figure 24 except for  $t = 24$  h.

convergence forcing is nearly twice as large in magnitude (Figure 27a-b). In the PBL case, convergence forcing is weak and negative within the PBL (due to lee slope PBL divergence) and positive in the convergence area near the top of the well-mixed layer (Figure 27d). The well-mixed layer extends through both the positive and negative forcing areas, so the effect of the convergence forcing field is unclear. The tilting effect, for example, is nearly neutral within the boundary layer at all times, but affects the surface front by forcing the potential temperature gradient at the top of the PBL. It is suspected that the PBL forcing term (equation (45)) counteracts the convergence forcing to some degree within the PBL. Overall, the convergence forcing in the PBL simulation is dramatically weaker on the lee slope than in the inviscid case.

The forcing fields at  $t = 42$  h are contained in Figure 28. The inviscid fields are complicated because of the gravity waves generated when the front reaches the base of the lee slope, but the forcing is nearly balanced at the front because the intensity is not changing in time at  $t = 42$  h (Figure 18). The PBL front is undergoing a gradual weakening trend from  $t = 36$  h to  $t = 48$  h. Strong frontolytic tilting forcing is present over the lower half of the lee slope (Figure 28d). The magnitude of the convergence forcing (again negative near the surface and positive near the PBL top) is considerably less than that of the tilting term. Deformation forcing is positive but a factor of ten smaller in magnitude. Thus the strong negative tilting effect is not balanced by positive convergence forcing as it is in the inviscid case and the PBL front weakens. Diffusive forcing is also probably a significant frontolytical factor in this region because the other forcing is relatively weak.



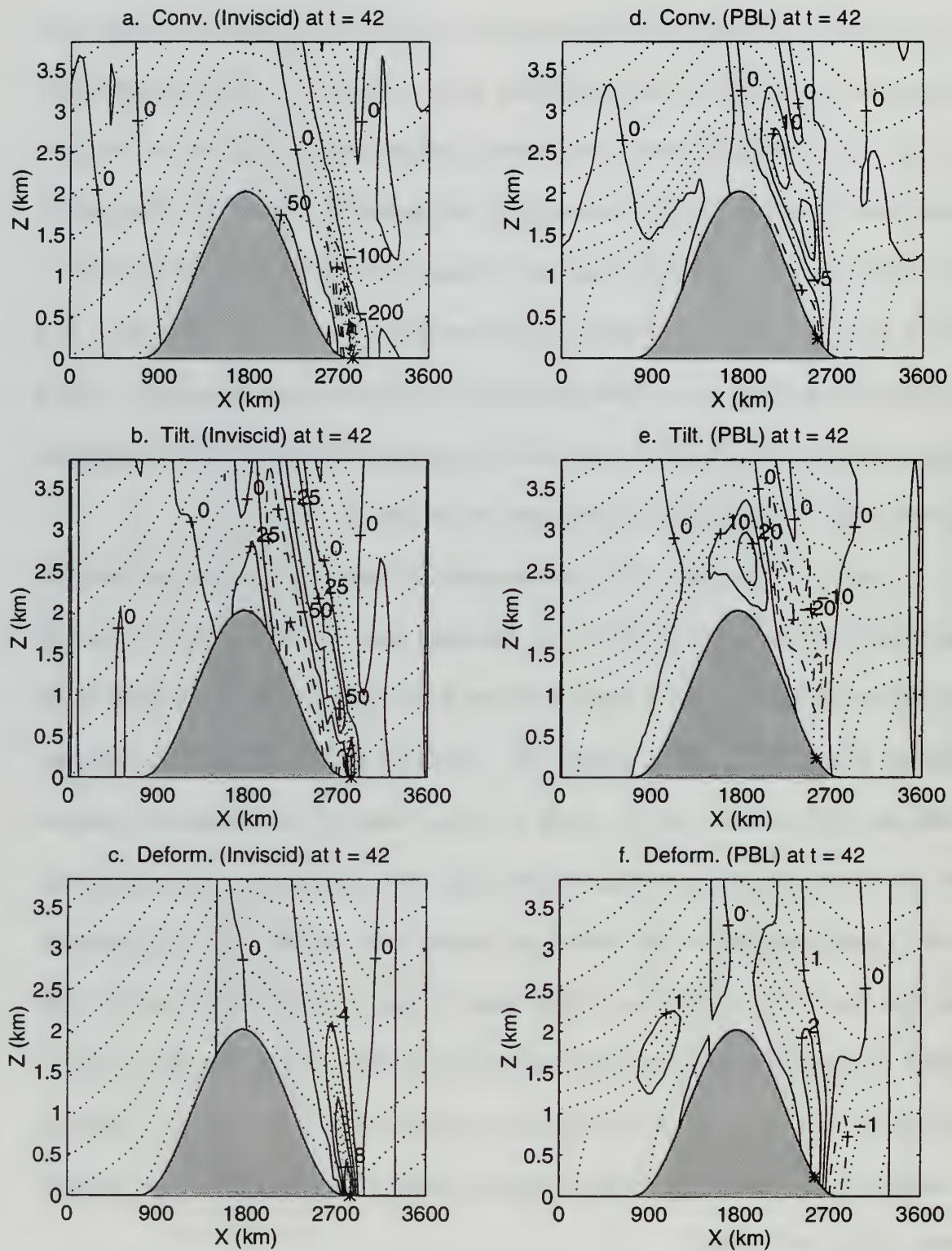


**Figure 28.** Same as Figure 24 except for  $t = 42$  h.

#### IV. SUMMARY OF RESULTS

The numerical simulations contained in this study demonstrate that the PBL plays an important role in frontal dynamics over mountainous topography. The effects in the flat topography case are consistent with those found in similar studies. In the mountain simulations, the elevation of the cross-ridge jet to the top of the PBL greatly reduces gravity wave generation and eliminates hydraulic jump effects in the mountain profiles considered. These results are more realistic than those of the W92 inviscid study, which generates more wave activity than is realistic for smooth, synoptic-scale ridges. The weaker elevated jet also results in much weaker lee slope convergence, which is the dominant forcing mechanism in the inviscid study. Turbulent mixing on the mountain slopes is shown to indirectly affect frontal dynamics. The PBL reaches higher  $\theta$ -levels on the ridge than on the adjacent planes, producing a horizontal temperature gradient in the well-mixed layer. This gradient has a large effect on frontal forcing because the convergence terms are proportional to the horizontal temperature gradient.

In summary, the front still shows frontolysis on the upwind slope and increased frontogenesis on the lee slope when PBL effects are included, but the magnitude of the variation is less than in the inviscid simulations. On the upwind slope, frictional convergence in the PBL *due to the mountain slope* combines with the mixing-enhanced horizontal temperature gradient. This produces a stronger front on the upwind slope and partially counteracts the weakening caused by the divergence associated with the accelerating cross-mountain flow above the PBL. At the crest of the ridge,



frontogenetical tilting is the dominant forcing mechanism and is weakened by the addition of the PBL. On the lee slope, convergence forcing is quite small or even negative in the PBL simulations because of reduced convergence associated with the cross-ridge jet and frictional divergence in the PBL near the surface. The result is that the PBL front intensifies much more slowly than in the inviscid case and begins to weaken over the lower half of the lee slope. In contrast to the inviscid simulations, the net effect of the front passing over the mountain is frontolytical when PBL effects are included. Narrower mountain profiles produce slightly different results because the fronts begin forming further upstream relative to the mountain, but the results are consistent over the ridge itself.

The study demonstrates the importance of the lower atmosphere in mountain dynamics. The vertical mixing of the PBL on sloping terrain produces unique effects and it is clear that the inclusion of a realistic PBL parameterization is even more critical in these frontogenesis simulations than in their flat topography counterparts. To complete the description of the frontogenetical forcing, the terms represented by equation (45) must be explicitly calculated. The vertical mixing effect depends heavily on the initial potential temperature distribution and future studies should also address this sensitivity. In particular, the inclusion of diurnal surface heating should have a major effect of frontal structure and dynamics. Also, the initial temperature state is not realistic in the PBL simulations, and the adjustment while the PBL forms may introduce extraneous frontal effects in the first stages of the integration. Similarly, the sensitivity to the boundary

layer constants, particularly the mixing length  $l$  should be addressed. Ultimately, the experiment should be expanded to a three-dimensional domain to evaluate the PBL effects on the along-ridge variations found by Gross (1994).



## LIST OF REFERENCES

- Arakawa, A., and V. R. Lamb, 1977: Computational design of the basic dynamical processes of the UCLA general circulation model. *Methods in Computational Physics*, Vol. 17, Academic Press, 174-264.
- Bannon, P. R., 1984: A semi-geostrophic model of frontogenesis over topography. *Beitr. Phys. Atmos.*, **57**, 393-408.
- Bannon, P. R., 1983: Quasi-geostrophic frontogenesis over topography. *J. Atmos. Sci.*, **40**, 2266-2277.
- Blackadar, A. K., 1978: High-resolution models of the planetary boundary layer. *Advances in Environmental Science and Engineering*, Vol. 1, J. R. Pfafflin and E. N. Ziegler, Eds., Gordon and Breach, 50-85.
- Blumen, W., 1980: A comparison between the Hoskins-Bretherton model of frontogenesis and the analysis of an intense surface frontal zone. *J. Atmos. Sci.*, **37**, 64-77.
- Blumen, W., and B. D. Gross, 1987: Advection of a passive scalar over a finite-amplitude ridge in a stratified rotating atmosphere. *J. Atmos. Sci.*, **44**, 1696-1705.
- Blumen, W., 1992: Propagation of fronts and frontogenesis versus frontolysis over orography. *Meteorol. Atmos. Phys.*, **48**, 37-50.
- Carruthers, D. J., and T. W. Choularton, 1982: Air flow over hills of moderate slope. *Quart. J. Roy. Meteor. Soc.*, **108**, 603-624.
- Carruthers, D. J., and J. C. R. Hunt, 1990: Fluid mechanics of airflow over hills: turbulence, fluxes, and waves in the boundary layer. *Atmospheric Processes over Complex Terrain*, W. Blumen, Ed., Amer. Meteor. Soc., 83-103.
- Davies, H. C., 1984: On the orographic retardation of a cold front. *Beitr. Phys. Atmos.*, **57**, 409-418.
- Dunst, M., and A. Rhodin, 1990: On the influence of frictional effects on surface fronts. *Beitr. Phys. Atmos.*, **63**, 223-242.
- Gross, B. D., 1994: Frontal interaction with isolated orography. *J. Atmos. Sci.*, **51**, 1480-1496.

- Hartsough, C. S., and W. Blumen, 1990: Objective cross-sectional analysis of diabatic circulation and vertical motions using ALPEX data. *Meteorol. Atmos. Phys.*, **43**, 221-230.
- Holt, T., and S. Raman, 1988. A review and comparative evaluation of multilevel boundary layer parameterizations for first-order and turbulent kinetic energy closure schemes. *Reviews of Geophysics*, Vol. 26, No. 4, Amer. Geo. Union, 761-780.
- Hunt, J. C. R., S. Leibovich, and K. J. Richards, 1988: Turbulent shear flow over hills. *Quart. J. Roy. Meteor. Soc.*, **114**, 1435-1470.
- Keyser, D., and R. A. Anthes, 1982: The influence of planetary boundary layer physics on frontal structure in the Hoskins-Bretherton horizontal shear model. *J. Atmos. Sci.*, **39**, 1783-1802.
- Mellor, G. L., and T. Yamada, 1974: A hierarchy of turbulence closure models for planetary boundary layers. *J. Atmos. Sci.*, **31**, 1791-1806.
- Merkine, L.-O., 1975: Steady finite-amplitude baroclinic flows over long topography in a rotating stratified atmosphere. *J. Atmos. Sci.*, **32**, 1881-1893.
- Ogura, Y., and N. A. Phillips, 1962: Scale analysis of deep and shallow convection in the atmosphere. *J. Atmos. Sci.*, **19**, 173-179.
- Pierrehumbert, R. T., and B. Wyman, 1985: Upstream effects of mesoscale mountains. *J. Atmos. Sci.*, **42**, 523-526.
- Radinovic, D., 1986: Analysis of ALPEX data, 20, 21 March and 24, 25, 30 April 1982. PSMP Report Series 22, WMO/TD No 154.
- Williams, R. T., M. S. Peng, and D. A. Zankofski, 1992: Effects of topography on fronts. *J. Atmos. Sci.*, **49**, 287-305.
- Yang, X., 1993: A nonhydrostatic model for simulation of airflow over mesoscale bell-shaped ridges. *Bound.-Layer Meteor.*, **65**, 401-425.
- Zehnder, J. A., and P. R. Bannon, 1988: Frontogenesis over a mountain ridge. *J. Atmos. Sci.*, **45**, 628-644.



## INITIAL DISTRIBUTION LIST

	No. Copies
1. Defense Technical Information Center 8725 John J. Kingman Rd., STE 0944 Ft. Belvoir, VA 22060-6218	2
2. Dudley Knox Library Naval Postgraduate School 411 Dyer Rd. Monterey, CA 93943-5101	2
3. Chairman, Code MR Meteorology Department Naval Postgraduate School Monterey, CA 93943	1
4. Prof. R. T. Williams, Code MR/Wu Meteorology Department Naval Postgraduate School Monterey, CA 93943	3
5. Prof. M. S. Peng, Code MR/Pg Meteorology Department Naval Postgraduate School Monterey, CA 93943	2
6. LCDR J. H. Powell 851 S. Taft St. Lakewood, CO 80228	2
7. Prof. W. Blumen Campus Box 391 University of Colorado Boulder, CO 80309	1



DUDLEY KNOX LIBRARY  
NAVAL POSTGRADUATE SCHOOL  
MONTEREY CA 93943-5101

DUDLEY KNOX LIBRARY



3 2768 00324254 6